

Spring 4-14-2017

Characterization of a Beam Position Monitor for Linear Accelerators

Artem Kuskov
University of New Mexico

Follow this and additional works at: https://digitalrepository.unm.edu/ece_etds



Part of the [Electrical and Computer Engineering Commons](#)

Recommended Citation

Kuskov, Artem. "Characterization of a Beam Position Monitor for Linear Accelerators." (2017). https://digitalrepository.unm.edu/ece_etds/343

This Thesis is brought to you for free and open access by the Engineering ETDs at UNM Digital Repository. It has been accepted for inclusion in Electrical and Computer Engineering ETDs by an authorized administrator of UNM Digital Repository. For more information, please contact disc@unm.edu.

Artem Kuskov

Candidate

Electrical and Computer Engineering

Department

This thesis is approved, and it is acceptable in quality and form for publication:

Approved by the Thesis Committee:

Dr. Salvador Portillo , Chairperson

Dr. Edl Schamiloglu

Dr. Christos Christodoulou

Dr. Gregory Dale

Characterization of a Beam Position Monitor for Linear Accelerators

by

Artem Kuskov

B.S., University of New Mexico, 2014

THESIS

Submitted in Partial Fulfillment of the
Requirements for the Degree of

Master of Science
Electrical Engineering

The University of New Mexico
Albuquerque, New Mexico

May, 2017

Dedication

To my American parents, Brent and Beth Hudson, for their love, support, and the priceless opportunity given to me to strive for the higher degree.

Acknowledgments

I want to thank my advisor Dr. Salvador Portillo for helping me with research, Dr Gregory Dale for supporting this project and giving me an opportunity to do research for a master's degree, Dr. Kip Bishofberger for giving me suggestions and helping me to overcome many obstacles . I also want to thank the Antennas Laboratory team, especially, Firas Ayoub and Arjun Gupta for taking their time to help me perform the experiment, and the LTD/HPM laboratory: Ahmed Elshafiey, Casey Rogers, and Thomas Schmidt, for their moral support. Last but not least, I want to thank my soon to be wife Brianna Davis for her tremendous moral support and always being there for me. Thank you all! I could not have done this work without you.

Characterization of a Beam Position Monitor for Linear Accelerators

by

Artem Kuskov

B.S., University of New Mexico, 2014

M.S., Electrical Engineering, University of New Mexico, 2017

Abstract

Los Alamos National Laboratory is one of the leaders in the development of accelerator based Mo-99 radioisotope production, a key diagnostic for medical applications. In order to increase the efficiency of Mo-99 yield, a non-interfering Beam Position Monitor (BPM) system was developed that measures the time dependent centering of the Bremsstrahlung producing electron beam. The Beam Positioning Monitor is comprised of 4 capacitive pickups positioned at 90 degrees to each other housed in a conflat 4.5 (63.5 mm) flange. This thesis develops, from first principles, analytical solutions for the transfer curve of this diagnostic based. Additionally, finite element time and frequency domain numerical models are developed for the behavior of the diagnostic under expected accelerator conditions. Finally, an experimental test bed was built and designed to characterize the behavior of the BPM under laboratory conditions.

Contents

List of Figures	viii
List of Tables	xii
1 Introduction	1
1.1 Introduction	1
1.2 The project overview and thesis goals	2
1.3 Thesis goals	5
2 Theoretical analysis	6
2.1 Introduction	6
2.2 Beam drifting in the tube	7
2.3 Beam positioning principle	9
2.4 Detailed model of the BPM	11
2.4.1 I_{pickup} derivation	11
2.4.2 Z_t derivation	14
2.4.3 V_{pickup} derivation	15
2.5 Circuit model	17
2.5.1 Transfer function derivation	18
2.5.2 Analytical capacitance calculation	20
2.5.3 Transfer function result	22
2.6 Conclusion	23
3 Numerical analysis	24
3.1 Introduction	24
3.2 The electrostatic analysis	25
3.2.1 Electrostatic simulation of C_{stray} and C_{pickup} for a pickup disk	26

Contents

3.2.2	Displacement analysis of a pickup with a stem	28
3.3	SPICE simulation	32
3.4	Transfer function simulation for an infinite line BPM	35
3.5	Frequency domain model of an experimental setup for BPM character- ization test stand	37
3.5.1	Case A. The ideal coaxial transmission line of length L	38
3.5.2	Case B. The ideal coaxial transmission line with an impedance mismatch section	39
3.5.3	Case C. 156 Ohm coaxial transmission line with 50 Ohm SMA port	47
3.5.4	Case D. The 156 Ohm line terminated with SMA ports at each end	48
3.5.5	Case E. A complete BPM setup	50
3.5.6	Case F. A complete BPM setup with conical reducers	53
3.6	Conclusion	54
4	Experimental analysis	56
4.1	Introduction	56
4.2	Experimental models	56
4.2.1	Experimental Configuration 1	57
4.2.2	Experimental Configuration 2	59
4.3	Experimental results for Configuration 1	60
4.4	Experimental results for Configuration 2	64
4.5	The experimental result comparison	67
4.5.1	The result comparison for Configuration 1	67
4.5.2	The result comparison for Configuration 2	71

Contents

4.6	Summary and conclusion	75
5	Conclusion and future work	78
5.1	Introduction	78
5.2	An analytical description of the BPM system	78
5.3	Numerical simulation models	80
5.4	The experimental setup	81
5.5	Future work	83

List of Figures

1.1	The Mo-99 production experimental setup schematic.	2
1.2	The Beam Position Monitor flange, SMA connectors for each pick up are shown at the numbered positions.	3
1.3	The conceptual accelerator schematic.	4
1.4	The beam represented as a macro pulse with multiple micro pulses.	4
2.1	Coaxial geometry represents an accelerator beam line.	6
2.2	A button Beam Position Monitor.	7
2.3	A schematic representation of an accelerator with a beam position monitor system.	8
2.4	Electric field lines of a charged particle beam moving at the velocity much less than the speed of light(a) and velocity close to speed of light(b).	9
2.5	XY-plane of the vacuum tube demonstrating the displacement of a beam.	10
2.6	A detailed schematic of the BPM system.	12
2.7	Equivalent BPM pickup circuit.	14
2.8	Simplified equivalent BPM pickup circuit.	15
2.9	Circuit representation of the BPM system.	18
2.10	A drawing for the current BPM design and its dimensions.	21
2.11	Frequency response of the BPM equivalent circuit.	22
3.1	The schematic of the BPM pickup-feed through connection.	24
3.2	Boundary conditions demonstration for electrostatic simulations. . .	26
3.3	A pickup disk in the BPM flange.	27

List of Figures

3.4	Pickup positions in the flange.(a)no displacement,(b) radial displacement, (c) recessed displacement,(d) protruded displacement. The displacements of pickups is 1 mm.	28
3.5	Change in stray capacitance as a function of radial pickup displacement.	29
3.6	Change in stray capacitance as a function of pickup recessed and protruded displacement.	30
3.7	Change in pickup capacitance as a function of recessed and protruded displacement.	32
3.8	Simplified circuit for the BPM system.	33
3.9	SPICE simulation of transfer functions for 4 pickup positions. Solid lines are magnitude values, dashed lines are phase values	34
3.10	A cross section of section for an infinitely long beamline.	35
3.11	Nominal position of a BPM pickup connected to a stub.	36
3.12	Transfer function result comparison of SPICE simulation vs CST simulation.	36
3.13	Case A. Coaxial transmission line with characteristic impedance of 50 Ohm.	38
3.14	Case A S-parameters for the coaxial transmission line with characteristic impedance of 50 Ohm.	39
3.15	Case B. A transmission line two different impedance values.	40
3.16	Case B. S-parameters for a coaxial line with two different characteristic impedance sections.	41
3.17	Case B. S-parameters results for S_{11} , S_{21} (fundamental mode) S_{21} (mode 4).	42
3.18	Port 2 mode visualization with simulated cutoff frequencies.	44
3.19	Path difference of real signal vs image signal concept.	45
3.20	50 Ohm port closeup.	46

List of Figures

3.21	Case C. 156 Ohm Beamline with SMA port.	47
3.22	Case C.S-Parameters for 156 Ohm Coaxial transmission line with 50 Ohm SMA port.	48
3.23	Case D geometry. The beamline is terminated at both ends with SMA ports.	49
3.24	Case D S-Parameters. Standing waves could be observed.	50
3.25	Case E Geometrical representation of BPM experimental setup.	51
3.26	Case E S-parameters for S_{11} , S_{21} , S_{31}	52
3.27	Case F Beamline with two conical reducers at each side.	53
3.28	Case F S-Parameters for the BPM system with conical reducers at each side.	54
4.1	The cross section of the experimental setup model.	57
4.2	The model of the experimental Configuration 1.	58
4.3	A detailed cutout of the experimental Configuration 1.	58
4.4	The model of the experimental Configuration 2.	59
4.5	The closeup of the experimental Configuration 2.	60
4.6	The measurement of S_{21} in configuration 1.	61
4.7	Measured S_{11} and S_{21} results in the configuration 1.	62
4.8	The measurement of S_{31} in the experimental Configuration 1.	63
4.9	Measured S_{31} result in the Configuration 1.	63
4.10	The measurement of S_{11} and S_{21} in Configuration 2.	64
4.11	Measured S_{31} result in the Configuration 1.	65
4.12	The measurement of S_{31} in Configuration 2	66
4.13	Measured S_{31} result in the Configuration 1.	66
4.14	Measured vs simulated S_{11} results comparison for the experimental Configuration 1.	67

List of Figures

4.15	Measured vs simulated S_{11} results comparison for the experimental configuration 1. The simulated plot is shifted 100 MHz to the left	68
4.16	Measured vs simulated S_{21} results comparison for the experimental Configuration 2.	68
4.17	Measured vs simulated S_{11} results comparison for the experimental Configuration 1. The simulated plot is shifted 100 MHz to the left.	69
4.18	Measured vs simulated S_{31} results comparison for the experimental Configuration 1.	70
4.19	Measured vs simulated S_{31} result comparison. The simulated plot is shifted 100 MHz to the left.	71
4.20	Measured vs simulated S_{11} results comparison for the experimental Configuration 2.	72
4.21	Measured vs simulated S_{11} results comparison for the experimental Configuration 2. The simulated result was shifted by 100 MHz to the left	72
4.22	S21 Measured vs simulated S_{21} results comparison for the experimental Configuration 2.	73
4.23	Measured vs simulated S_{21} results comparison for the experimental configuration 2. The simulated result was shifted by 100 MHz to the left.	74
4.24	Measured vs simulated S_{31} results comparison for the experimental Configuration 2.	74
4.25	Measured vs simulated S_{31} results comparison for the experimental Configuration 2. The simulated result was shifted by 100 MHz to the left.	75

List of Tables

3.1	Capacitance and calculated cutoff frequency results for 4 pickup position cases.	33
3.2	Values of p'_{nm} for TE modes of a Circular waveguide	43
3.3	Values of p_{nm} for TM modes of a Circular waveguide	43

Chapter 1

Introduction

1.1 Introduction

In 1928, a Norwegian accelerator physicist Rolf Wideröe built the first linear accelerator using the principle of alternating voltage inside of a tube, which led to the acceleration of charged particles [1]. Linear accelerator technologies developed for particle and nuclear physics research has led to a deeper understanding of material properties, at the molecular and atomic level [2]. Additionally, linear accelerators are not bound to the laboratory. They have found uses in the medical field, by providing lifesaving radiation for cancer treatment as well as in the production of radioisotopes to aid in the diagnosis of life threatening diseases [3]. One of these radioisotopes, Mo-99, can easily bind to cancer cells and once bound radiation sensors will pick the areas of radioisotope decay which directly correlate to cancerous regions within the body [4] [5]. Mo-99 has been typically produced in nuclear reactors utilizing highly enriched uranium. The highly enriched uranium, although produced in the USA must be transferred to foreign countries which produce Mo-99 [6]. This is a problem as now highly enriched uranium, which can be used for weapons development, could potentially be lost or misused [7]. Additionally, several countries, for example Canada, are shutting down their nuclear reactor radioisotope efforts and a new technology, free from proliferation concerns must be found. Linear accelerators can be this technology by generating bremsstrahlung of high enough energies such that these photons can convert Mo100 to Mo-99 [8].

1.2 The project overview and thesis goals

Los Alamos National Laboratory, one of the world leaders in radioactive isotopes generation via linear accelerators, are working on developing a robust and efficient Mo-99 radioisotope process based on linear accelerator technology. The process calls for the production of high energy Bremsstrahlung, greater than 20 MeV, by bombarding a high Z material (which is a large nucleus material such as Tungsten) with a high current small diameter electron beam. The resultant Bremsstrahlung is incident on a Mo-100 target and through a photonuclear reaction, where the high energy X-rays interact with the nucleus, a neutron is produced along with Mo-99 [9]. The cross section for photonuclear reaction is relatively low and it is critical that the highest flux of electrons impinge on the target [10]. It is then crucial to ensure that the beam is properly centered along the beam path if one is to maximize the efficiency of isotope production.

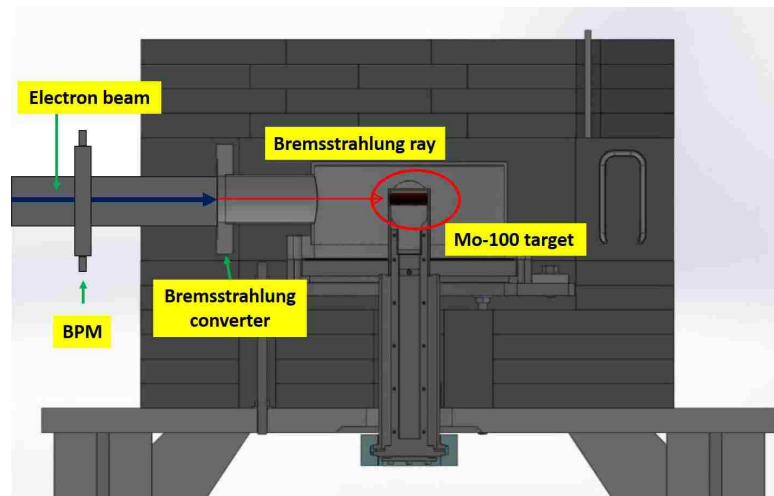


Figure 1.1: The Mo-99 production experimental setup schematic.

The schematic shown in Figure 1.1 shows the working principle of the Mo-99 production. The red arrow represents the electron beam aimed at the high Z material

Chapter 1. Introduction

target to produce high energy photons. The Mo-100 target consists of 25 disks, stacked sequentially in the housing. The diameter of each disk is 12 mm; therefore, for the most accurate impingement of the electron beam on the Bremsstrahlung producer, a diagnostic tool, called the Beam Position Monitor (BPM), is needed to ensure that the beam is centered on target [9].

The BPM system was designed and manufactured into a zero length conflat flange and is shown in Figure 1.2. The flange has the outer diameter $R_o = 4.5''$ (114.3mm), the inner diameter $R_i = 2.5''$ (63.5mm), 8 holes and 4 BPM pickups installed 90 deg offset from each other. The following configuration produces a compact diagnostic in the experimental setup.



Figure 1.2: The Beam Position Monitor flange, SMA connectors for each pick up are shown at the numbered positions.

The accelerator consists of four main parts as shown in Figure 1.3 : electron injector, acceleration region, free drift space and target region. The electron injector produces beam bunches, which are then accelerated with a series of klystrons in the S band to

Chapter 1. Introduction

energies up to 42 MeV. After acceleration, electrons propagate in the free drift space, where the position of the beam can be controlled with quadrupole magnets before the beam hits the target [11].

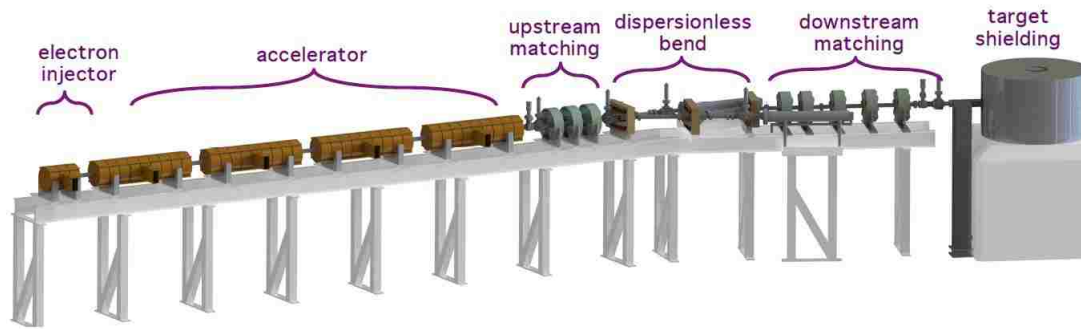


Figure 1.3: The conceptual accelerator schematic.

The beam bunches have a macro pulse with a period of $5 \mu s$ based on the repetition rate of the electron injector. The macro pulse of the beam, however, is comprised of micro pulses, as shown in Figure 1.4, with pulse width of 0.36 ns based on the operating frequency of klystrons.

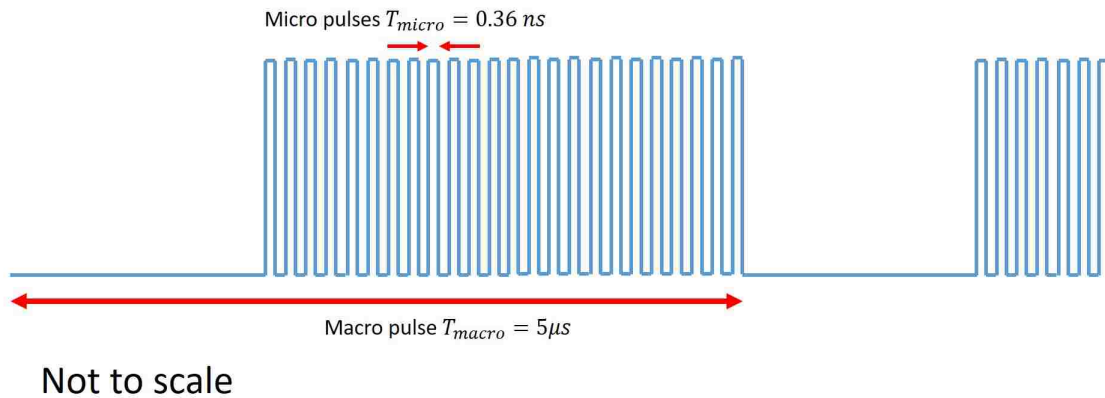


Figure 1.4: The beam represented as a macro pulse with multiple micro pulses.

1.3 Thesis goals

The goal of the project is to create an experimental test bed which emulates a short section of a drift space and fully characterize the behavior of a provided BPM diagnostic under following conditions:

Beam energy: $V_{peak} = 42 \text{ MeV}$

Average power: $P_{avg} = 120 \text{ kW}$

Beam repetition rate (Macro pulse): $T_{beam} = 5 \mu s$

Beam peak width (Micro pulse): $T_{peak} = 0.36 \text{ ns}$

Frequency band: *S band* $[2 - 4] \text{ GHz}$

Operating frequency $f_{operating} = 2.8 \text{ GHz}$

The characterization is done in threefold: First to create an analytical description of the transfer curve of operation for BPM from first physical and mathematical principles. Second to develop, finite element time domain and frequency domain models to simulate the behavior of the BPM exposed to typical beam line parameters and to model the response of the BMP under these inputs. Finally, a coaxial static test bed was designed and built to allow for the experimental measurement of the BPM transfer curve under various operating conditions.

Chapter 2

Theoretical analysis

2.1 Introduction

Most charged particle accelerators have a common cylindrical geometry which allows beam bunches to propagate uniformly in the center of the beam line. The analogy is the closest to a coaxial transmission line, where a beam acts as an inner conductor with radius r_{beam} and a guiding beam line acts as an outer conductor with radius $r_{beamline}$. Figure 2.1, demonstrates the visual representation of the coaxial transmission line. For the purpose of this document, the coaxial geometry is used to describe and derive relationships between a beam, a beamline, and a beam position monitor system.

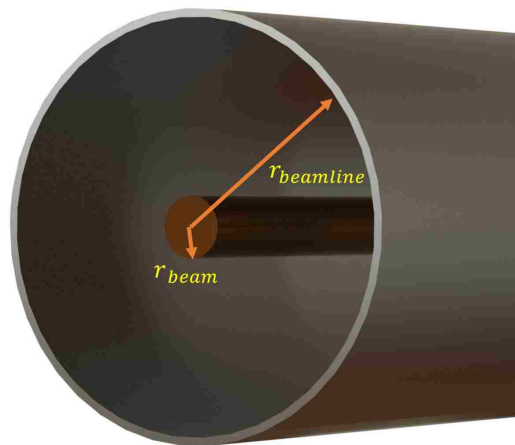


Figure 2.1: Coaxial geometry represents an accelerator beam line.

For some sections of the theoretical analysis beampipe - beam interaction is described with an assumption that accelerator line is very long and only a section is being described. Further in the document, the infinitely long beamline assumption is softened and an experimental prototype for a Beam Position Monitor is described.

2.2 Beam drifting in the tube

While the beam bunch drifts inside of the accelerator chamber, it produces electric and magnetic fields. The magnitude of an electric field depends on the amount of total charge in the beam bunch. The linear charge distribution is related to the length of the beam bunch as well as the position of the beam bunch inside the chamber. As the beam travels, an image charge travels along on the inner surface of the beam line. The movement of image charges is called an image current I_{image} .

The beam bunch traveling ideally in the middle of the beam chamber, produces an image current uniform on the beam pipe surface; however, when the beam is off-center and closer to the wall, the magnitude of the image current at that region increases which is called a proximity effect [12].

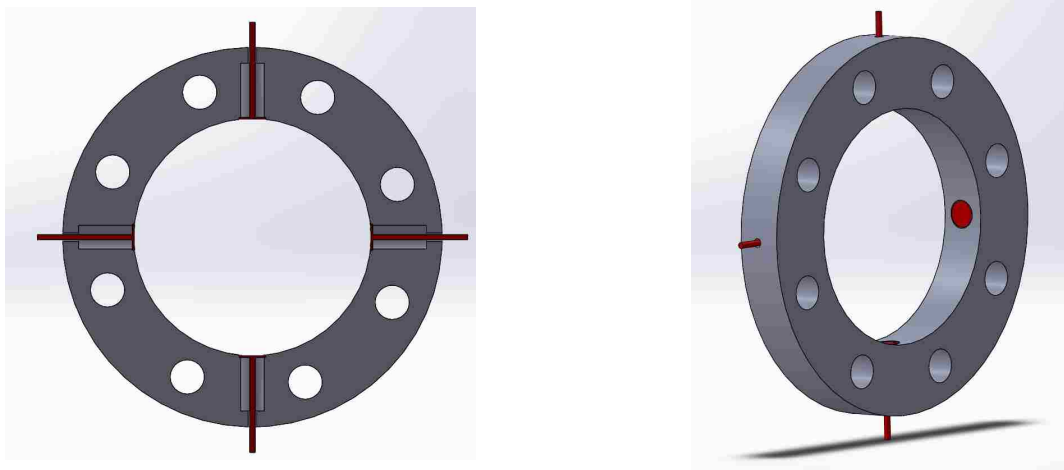


Figure 2.2: A button Beam Position Monitor.

The proximity effect is a mechanism that allows a beam position to be measured. Such measurement systems are called the Beam Position Monitors or BPM. There are several different types of Beam position monitors, but for the purpose of this document only "button" BPMs are discussed since different types of Beam position

monitors use different working principles and different geometries.

As shown in figure 2.2, BPM electrodes (pickups) are installed in pairs on the opposite ends of the flange flush with the surface to maintain the uniform image charge flow on the surface of the beam line. A detailed description of the beam spatial position is described in Section 2.3.

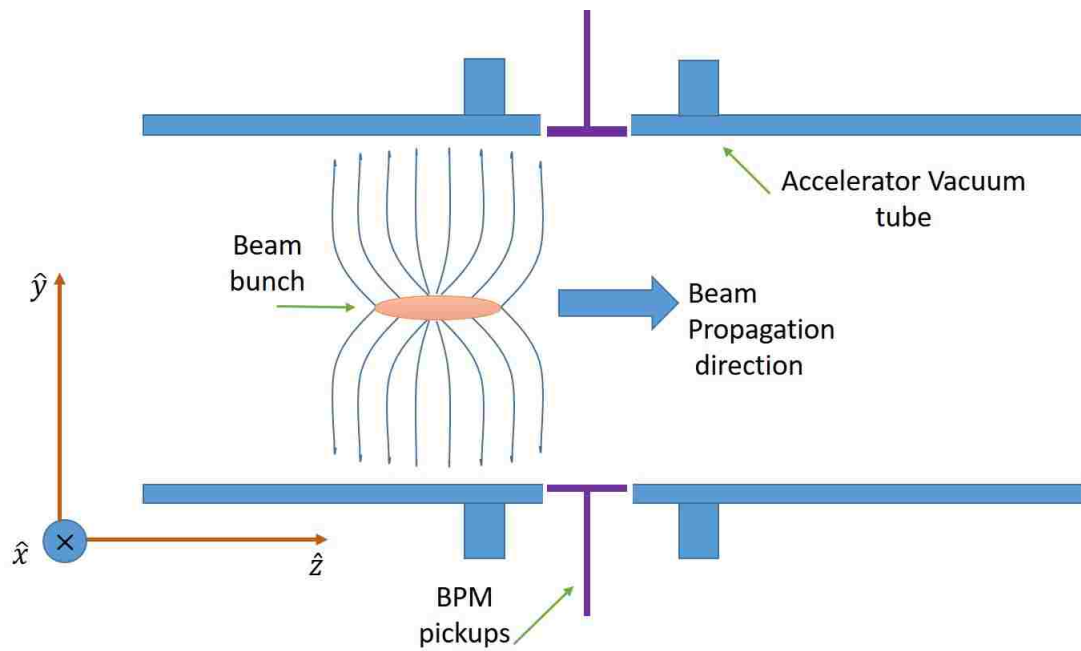


Figure 2.3: A schematic representation of an accelerator with a beam position monitor system.

In order to demonstrate the principle of a beam drifting in a tube refer to Figure 2.3, which demonstrates a 2-D schematic of a beam vacuum tube. The pink oval in the figure is representative of a beam bunch traveling longitudinally in the vacuum chamber. Electric field lines extend radially and usually are normal to the beam pipe.

BPMs are used in different regimes such as high velocity beams and low velocity beams [13]. Electric field lines propagate information at the speed of light; however, when the beam's velocity approaches the speed of light, the electric field lines

experience Lorentz transformation as shown in Figure 2.4 [13]. The energy of the beam, used for this thesis, is about 42 MeV, which requires relativistic effects to be taken into account.

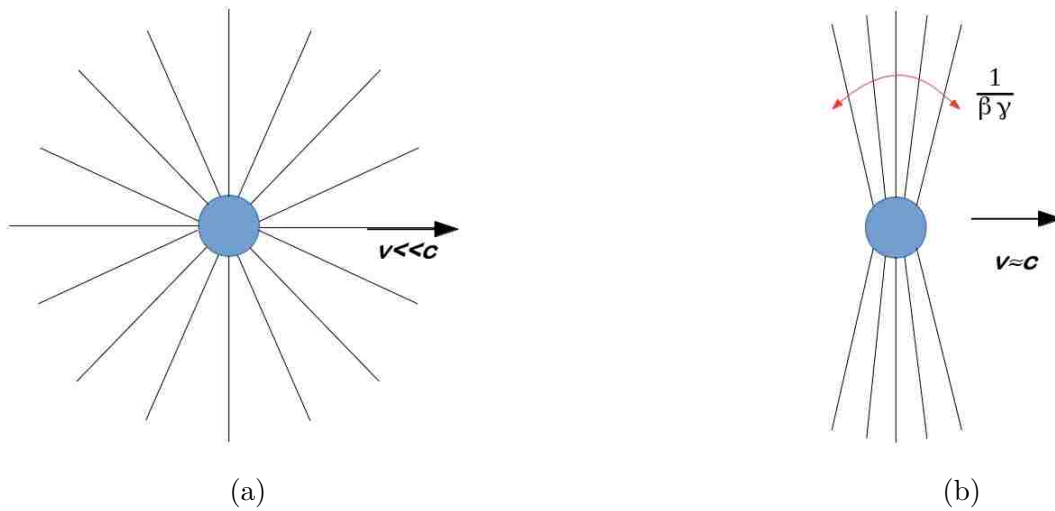


Figure 2.4: Electric field lines of a charged particle beam moving at the velocity much less than the speed of light(a) and velocity close to speed of light(b).

2.3 Beam positioning principle

As described in the previous section, the beam position in space could be measured with a time variant image charges on the surface of installed electrodes. A BPM, described in Section 1.2, has two sets of electrodes for measuring vertical and horizontal positions of the beam, as shown in Figure 2.5. All electrodes are flush with the surface, but for the demonstration purpose, the pickups are shown slightly displaced towards the beam.

Chapter 2. Theoretical analysis

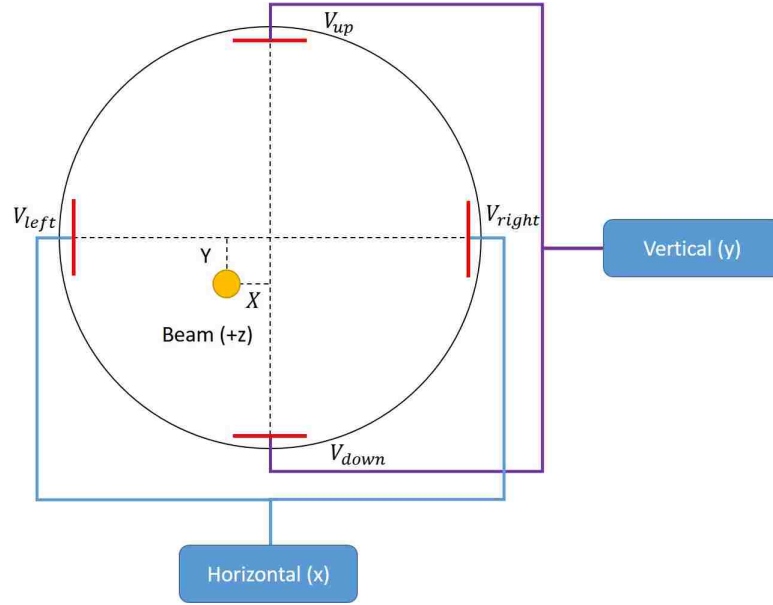


Figure 2.5: XY-plane of the vacuum tube demonstrating the displacement of a beam.

For a small beam deviation from the center, a difference in signals could be calculated using Equations 2.1 and 2.2.

$$\Delta V_x = V_{right} - V_{left} \quad (2.1)$$

$$\Delta V_y = V_{up} - V_{down} \quad (2.2)$$

However, when the deviation of the beam from the center is greater than $\frac{1}{4}$ of the beam pipe radius, non-linear effects occur and the position calculation becomes more complicated. See Equations 2.3 and 2.4.

$$X = \frac{1}{S_x} * \frac{V_{right} - V_{left}}{V_{right} + V_{left}} \quad (2.3)$$

$$Y = \frac{1}{S_y} * \frac{V_{up} - V_{down}}{V_{up} + V_{down}} \quad (2.4)$$

$$(2.5)$$

Where X and Y are normalized distances of the beam deviation from the center in mm, S_x and S_y are position sensitivity parameters measured in $\%/mm$.

$$S_x = \frac{d}{dx} \left(\frac{\Delta V_x}{\Sigma V_x} \right) \quad (2.6)$$

$$S_y = \frac{d}{dy} \left(\frac{\Delta V_y}{\Sigma V_y} \right) \quad (2.7)$$

2.4 Detailed model of the BPM

The previous section showed that for the beam position calculation calls for the derivation of the voltage V_{pickup} in terms of the beam current and pickup geometric parameters [14]. Based on Ohms law an expression for V_{pickup} could be shown:

$$V_{pickup} = I_{pickup} Z_t \quad (2.8)$$

Where I_{pickup} is the pickup current and Z_t is the transfer impedance of the pickup. Figure 2.6 shows the detailed schematic of the BPM- beam interaction, which will act as a visual guide for V_{pickup} , I_{pickup} , and Z_t derivations. Due to the complexity of the derivation, first, it is assumed that the beam is ideally in the center.

2.4.1 I_{pickup} derivation

First an analytical expression for I_{pickup} is derived. A beam bunch moving inside of the beam pipe contains the total charge Q_{beam} . The electric field of the beam bunch induces charges on the surface of the vacuum pipe. A total charge on the pickup Q_{pickup} changing with respect to time is proportional to a total beam current. The pickup with radius r_{pickup} is flush with the surface of the beam pipe; therefore, the surface charge density of a short section of a beamline σ_{duct} is the same as the surface charge density of the pickup σ_{pickup} .

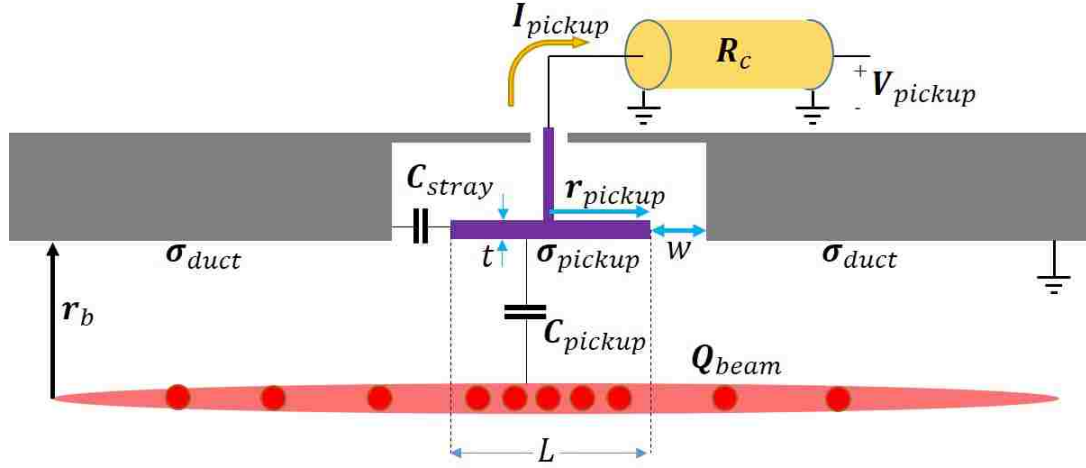


Figure 2.6: A detailed schematic of the BPM system.

The surface charge density σ_{duct} represents the total charge distribution on the surface area of a duct A_{duct} . The surface charge density of the duct can be related to the total beam charge Q_{beam} with the following expression:

$$\sigma_{duct} = \frac{Q_{beam}}{A_{duct}} \quad (2.9)$$

Where $A_{duct} = 2\pi r_b L$ is the surface area of the beamline section of length L . The total charge on the pickup is Q_{pickup} , therefore the surface charge density on the pickup is:

$$\sigma_{pickup} = \frac{Q_{pickup}}{A_{pickup}} \quad (2.10)$$

Where $A_{pickup} = \pi r_{pickup}^2$ is the surface area of BPM pickup. Due to the pickup positioned flush with the beamline $\sigma_{duct} = \sigma_{pickup}$, that allows the following relation to be described:

$$Q_{pickup} = \frac{\pi r_{pickup}^2}{2\pi r_b L} Q_{beam} \quad (2.11)$$

Chapter 2. Theoretical analysis

As noticed the Q_{pickup} is a fractional charge distribution of the total beam charge Q_{beam} . A geometric factor K could be used instead given by:

$$Q_{pickup}(t) = KQ_{beam}(t) \Rightarrow \frac{dQ_{pickup}(t)}{dt} = K \frac{dQ_{beam}(t)}{dt} \quad (2.12)$$

where

$$K = \frac{r_{pickup}^2}{2r_b L}$$

Since the beam is relativistic, the linear charge density has to be taken into account for the correct pickup current derivation. As shown on Figure 2.6, the area of interest is the beam section of length L . A linear charge density could be described in a following way:

$$\lambda_{beam}(t) = \frac{1}{v_{beam}} I_{beam}(t) \Rightarrow Q_{beam} = \frac{L}{\beta c} I_{beam}(t) \quad (2.13)$$

Differentiating both sides of the previous equation, with respect to time, results in

$$\frac{dQ_{beam}(t)}{dt} = \frac{L}{\beta c} \frac{dI_{beam}(t)}{dt} \quad (2.14)$$

Finally, the relation between beam current and pickup current is described below

$$I_{pickup}(t) = K \frac{L}{\beta c} \frac{dI_{beam}(t)}{dt} \quad (2.15)$$

A Fourier transform could be used to convert the problem to frequency domain

$$\frac{dI_{beam}(t)}{dt} \Leftrightarrow i\omega \widehat{I}_{beam}(\omega) \quad (2.16)$$

Chapter 2. Theoretical analysis

where $\hat{I}_{beam} = I_{beam}e^{i\omega t}$

At last I_{pickup} is obtained in terms of beam current

$$I_{pickup}(\omega) = K \frac{L}{\beta c} i\omega I_{beam}(\omega) \quad (2.17)$$

2.4.2 Z_t derivation

The second variable that is derived is the transfer impedance of the pickup Z_t . Figure 2.7 demonstrates the equivalent circuit of the pickup. In this case the pickup current is represented as a source, C_{stray} and R_c are making up the transfer impedance Z_t .

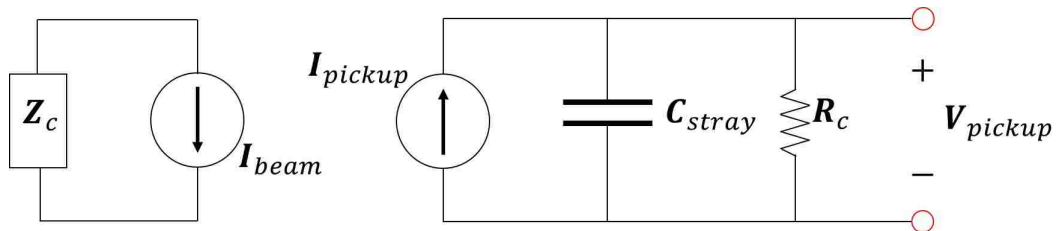


Figure 2.7: Equivalent BPM pickup circuit.

Z_t could be rewritten more compactly yielding the following simplified circuit

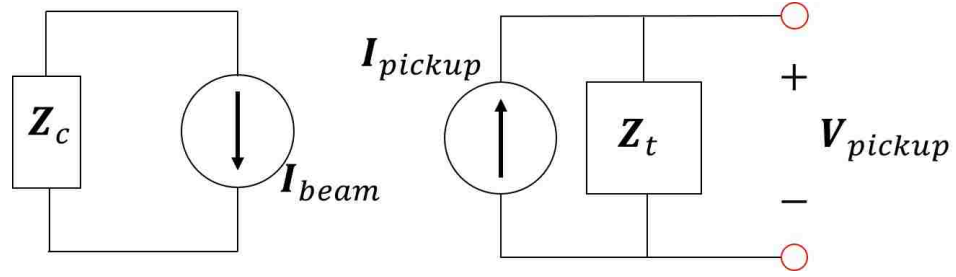


Figure 2.8: Simplified equivalent BPM pickup circuit.

To simplify the calculation, the calculation of Z_t is expressed in frequency domain.

The reactance of the capacitor is

$$X_c = \frac{1}{i\omega C}$$

The combination of R_c and C_{stray} solves the transfer impedance to be

$$Z_t = C_{stray} || R_c = \frac{R_c}{1 + i\omega R_c C_{stray}} \quad (2.18)$$

2.4.3 V_{pickup} derivation

Now, when expressions for I_{pickup} and Z_t were solved, it is possible to find V_{pickup}

$$V_{pickup}(t) = I_{pickup}(t)Z_t(t) \iff V_{pickup}(\omega) = \hat{I}_{pickup}(\omega)Z_t(\omega) \quad (2.19)$$

Substituting results for I_{pickup} and Z_t results in

$$V_{pickup}(\omega) = \frac{R_c}{1 + i\omega R_c C_{stray}} I_{pickup} \Rightarrow \frac{KL}{\beta c} \frac{R_c}{1 + i\omega R_c C_{stray}} i\omega \hat{I}_{beam}(\omega) \quad (2.20)$$

By observation, the cutoff frequency of the circuit described by 2.7 is

$$\omega_c = \frac{1}{R_c C_{stray}}$$

Chapter 2. Theoretical analysis

and equation 2.20 can be written in terms of the cutoff frequency

$$V_{pickup} = \frac{KL}{\beta c} \frac{1}{C_{stray}} \frac{i\omega R_c C_{stray}}{1 + i\omega R_c C_{stray}} \hat{I}_{beam}(\omega) \quad (2.21)$$

The above equation could have more convenient form by replacing ω_c to get the following

$$V_{pickup} = \frac{KL}{\beta c} \frac{1}{C_{stray}} \frac{\frac{i\omega}{\omega_c}}{1 + \frac{i\omega}{\omega_c}} \hat{I}_{beam}(\omega) \quad (2.22)$$

Equation 2.22 demonstrates a pickup voltage in terms of the transfer impedance and the pickup current; however, it could be seen that the transfer impedance could operate differently in different regions of ω . For that step, an absolute magnitude of the transfer impedance needs to be found

$$|Z_t| = \frac{KL}{\beta c C_{stray}} \frac{\frac{\omega}{\omega_c}}{\sqrt{1 + \frac{\omega^2}{\omega_c^2}}} \quad (2.23)$$

Transfer impedance behavior at different ω regions needs to be addressed separately.

At $\omega \gg \omega_c$

$$Z_t \propto \frac{\frac{i\omega}{\omega_c}}{1 + \frac{i\omega}{\omega_c}} \rightarrow 1 \quad (2.24)$$

therefore the pickup voltage could be rewritten in terms of beam current as

$$V_{pickup}(\omega) = \frac{\pi r_{pickup}^2}{2\pi r_b} \frac{1}{\beta c} \frac{1}{C_{stray}} \hat{I}_{beam}(\omega) \quad (2.25)$$

At $\omega \ll \omega_c$

$$Z_t \propto \frac{\frac{i\omega}{\omega_c}}{1 + \frac{i\omega}{\omega_c}} \rightarrow \frac{i\omega}{\omega_c} \quad (2.26)$$

the pickup voltage in terms of beam current becomes

$$V_{pickup}(\omega) = \frac{\pi r_{pickup}^2}{2\pi r_b} \frac{R}{\beta c} i\omega \hat{I}_{beam}(\omega) \quad (2.27)$$

The observation could be made that in a region, where the operating frequency is much higher than the cutoff frequency, the pickup voltage depends on the stray capacitance, but the current does need integration. In the regime where the operating frequency is much lower than the cutoff frequency, the pickup voltage becomes independent of the stray capacitance.

Since the goal of the project is the full characterization of the provided BPM, the analytical approach described above, introduces difficulties to the characterization process. I_{pickup} needs to be derived for every case of the beam displacement, which would affect V_{pickup} . An additional analytical model was developed based on a circuit model.

2.5 Circuit model

As described in the previous section, the position of the beam heavily influences the derivation of I_{pickup} , which complicates the characterization of the BPM. Based on Figure 2.6 the BPM system could be expressed with a simple equivalent circuit shown in Figure 2.9, where C_{pickup} is the capacitive coupling between the beam and the pickup, C_{stray} is the parasitic capacitance between the pickup and the body of the flange and R_c is the characteristic impedance of a transmission line connected to a pickup.

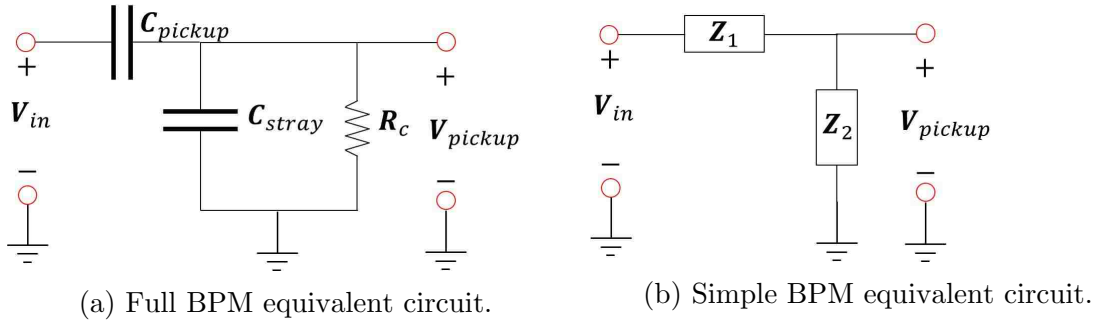


Figure 2.9: Circuit representation of the BPM system.

Since C_{stray} depends on the position of the pickup inside of the flange, and R_c has a constant characteristic impedance, the only parameter that would change as a function of the beam displacement is C_{pickup} . For the following approximation of C_{pickup} , the beam is assumed to have a cylindrical shape and a fixed radius r_{beam} , which is described in more detail later in the chapter. The transfer function of the following circuit model fully characterizes the BPM analytically [15].

2.5.1 Transfer function derivation

The transfer function needs to be derived as a function of frequency; therefore, circuit components should be derived in the frequency domain where $s = i\omega$, therefore the reactance values for capacitor C_{pickup} and C_{stray} are X_1 and X_2 and are expressed by:

$$X_1 = \frac{1}{sC_{pickup}} \quad (2.28)$$

$$X_2 = \frac{1}{sC_{stray}} \quad (2.29)$$

The complex impedance is expressed as $Z = R + X$, where R is the resistance and X is the reactance of the circuit. For Z_1 there is no resistance component and therefore $Z_1 = X_1$. The complex impedance Z_2 will be $C_{stray} || R$

Chapter 2. Theoretical analysis

$$Z_2 = \left(\frac{1}{R} + sC_{stray} \right)^{-1} \Rightarrow \frac{R}{sRC_{stray} + 1} \quad (2.30)$$

Finally, $V_{pickup} = V_{in} \left(\frac{Z_2}{Z_1 + Z_2} \right)$, therefore to solve for $H(s) = \frac{V_{pickup}}{V_{in}}$ all related components need to be substituted. The result yields:

$$H(s) = \frac{V_{pickup}}{V_{in}} = \frac{sR_c C_{pickup}}{sR_c(C_{pickup} + C_{stray}) + 1} \quad (2.31)$$

There an explanation for this

$$H(i\omega) = \frac{i\omega R_c C_{pickup}}{i\omega R_c(C_{pickup} + C_{stray}) + 1} \quad (2.32)$$

For simplicity let

$$a = R_c C_{pickup}$$

and

$$b = R_c(C_{stray} + C_{pickup})$$

Substituting these factors back in Equation 2.32, the following equation is obtained

$$H(i\omega) = \frac{i\omega a}{i\omega b + 1} \quad (2.33)$$

Next, the equation gets divided into real and imaginary parts:

$$H(i\omega) = \frac{\omega^2 ab}{1 + \omega^2 b^2} + i \frac{\omega a}{1 + \omega^2 b^2} \quad (2.34)$$

The absolute value of the transfer function is

$$|H(\omega)| = \frac{\omega a}{\sqrt{1 + \omega^2 b^2}} \quad (2.35)$$

Chapter 2. Theoretical analysis

The transfer function behavior at infinity

$$\lim_{\omega \rightarrow \infty} |H(\omega)| = \frac{a}{b} \quad (2.36)$$

To calculate the cutoff frequency $H\omega_{cut}$ we need to make the absolute value equal to $\frac{H(\infty)}{\sqrt{2}}$

$$\omega_c = \frac{1}{b} = \frac{1}{R(C_{stray} + C_{pickup})} \quad (2.37)$$

Finally the cutoff frequency demonstrates the behavior of the circuit acting like a high pass filter.

$$f_c = \frac{1}{2\pi R_c(C_{stray} + C_{pickup})} \quad (2.38)$$

2.5.2 Analytical capacitance calculation

The next step in plotting the transfer function for the circuit is to calculate capacitance values for C_{stray} and C_{pickup} analytically. Figure 2.10 demonstrates a schematic of the BPM flange with dimensions, which are used to calculate C_{stray} as well as C_{pickup} . The capacitance C_{stray} is estimated as that of a short coax formed by the button and the beam pipe inner walls [16] .

$$C_{ideal} = \frac{2\pi\epsilon_0}{\ln\left(\frac{r_{pickup+w}}{r_{pickup}}\right)} t \quad (2.39)$$

Chapter 2. Theoretical analysis

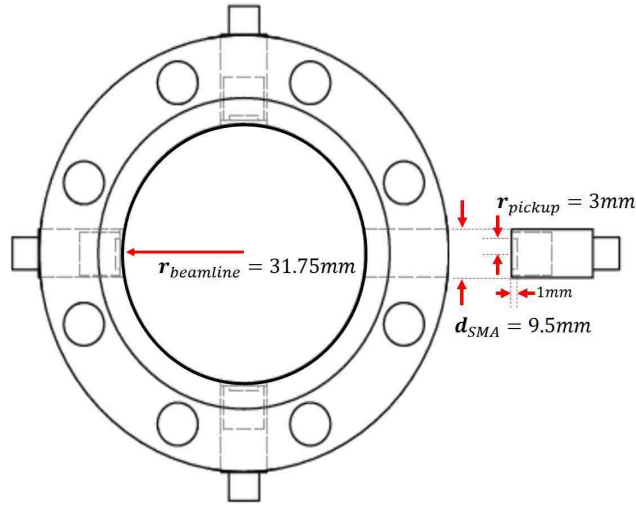


Figure 2.10: A drawing for the current BPM design and its dimensions.

Where r_{pickup} is the radius of pickup w is the gap distance between the pickup and the annular cut, ϵ_0 is a permittivity of free space, and t is the thickness of the pickup.

For stray capacitance calculations we have the following parameters:

$$r_{SMA} = 4.75[mm], r_{in} = 3[mm], \epsilon_r = 1, t = 1mm, w = 1.75mm$$

$$\text{Therefore } C_{stray} = 0.121 [pF]$$

As mentioned before the C_{pickup} calculation could be approximated using a capacitance of a coaxial line[17]. This calculation involves a volume region of beamline of the length equal to the pickup diameter $2r_{pickup}$, the capacitance in this region is referred to as C_{duct} [17].

$$C_{duct} = \frac{2\pi\epsilon_0}{\ln\left(\frac{r_b}{r_{beam}}\right)} * 2r_{pickup} = 0.131 * 10^{-12} F \quad (2.40)$$

Where C_{duct} is capacitance of the beam to the region of inner surface area of the beamline, $r_b = 31.75[mm]$ is the beamline radius, $r_{beam} = 2.35[mm]$ is the beam radius and $r_{pickup} = 3[mm]$ is the pickup radius.

Chapter 2. Theoretical analysis

The capacitance of a single pickup is proportional to the fractional surface area of the pickup with respect to the surface area of the duct.

Capacitance of each individual pickups to the beam in the center yields to be

$$C_{pickup}(each) = KC_{duct} = 3.1 * 10^{-15} F \approx 3fF \quad (2.41)$$

The analytical calculation of the capacitance values for C_{stray} and C_{pickup} are based on approximations under ideal configurations and may not be accurate due to fringing fields and need to be verified with numerical simulation tools in next chapters.

2.5.3 Transfer function result

With capacitance values the transfer function, finally, can be plotted.

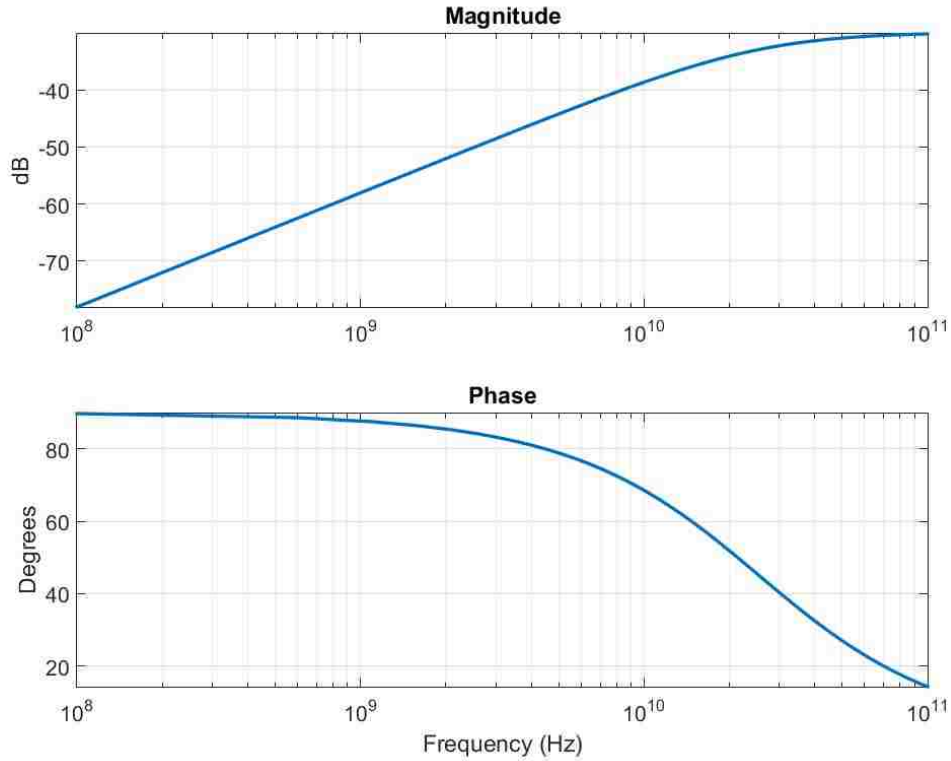


Figure 2.11: Frequency response of the BPM equivalent circuit.

The transfer function of the circuit is shown on Figure 2.11, which summarizes the analytical characterization of the BPM. The frequency range is set from 100 MHz to 100 GHz to demonstrate the asymptotic value of the of the transmission line. The circuit acts as a high pass filter with a cutoff frequency calculated by equation 2.38; nevertheless, as mentioned before the analytically calculated capacitance values may not be accurate due to model approximations and a numerical finite element code will be used in the next chapter for an accurate capacitance calculation.

2.6 Conclusion

The goal of Chapter 2 was to characterize the BPM analytically from first physical and mathematical principles. The initial approach for the characterization was to derive an expression for V_{pickup} . The derivation was based on the condition for the beam positioned ideally in the center of the beamline, that was not enough to characterize the BPM for every position of the beam and the expression for V_{pickup} needed to be derived every time from scratch. Instead, a slightly different approach was applied to the problem, producing the equivalent electrical circuit of the BPM system. The circuit model included three main variables: C_{pickup} -the capacitive coupling between the beam and the pickup, C_{stray} -the parasitic capacitance between the pickup and the body of the flange and R_c - the characteristic impedance of a transmission line connected to a pickup. Based on the BPM equivalent circuit model a transfer function was derived. The transfer function provided the necessary information for the BPM characterization as a function of the operating frequency. The next chapter will focus on the numerical simulations for the transfer function to support analytical findings.

Chapter 3

Numerical analysis

3.1 Introduction

The previous chapter focused on a Beam Position Monitor description from physical and mathematical principles. The following chapter focuses on the generation of numerical simulation models of BPM setup using an Electrostatic finite element solver, a Frequency domain solver and SPICE simulation codes.

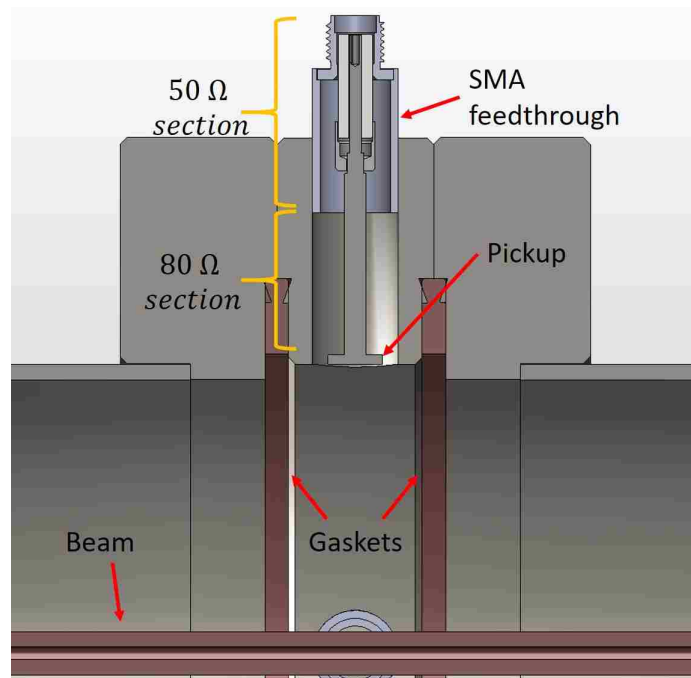


Figure 3.1: The schematic of the BPM pickup-feed through connection.

In order to correctly create the model of the BPM, a closer look at the BPM connection needs to be taken. Figure 3.1 shows the cutaway schematic of the pickup connection. The SMA feed through is welded to a small stem, which is welded to the

pickup button. The SMA feed through divides the transmission line of the pickup into 2 regions with different impedances: a 50 Ohm section (the SMA feed through) and a 80 Ohm section (the stem region). A well matched transmission line accounts for any stray capacitances that are a part of the transmission line, but since there exist a region of the impedance mismatch, the capacitance of that transmission line will contribute to C_{stray} [16],[18]. The previous chapter discussed C_{stray} as the parasitic capacitance of the pickup disk only. The following chapter will add the capacitance of the stem up to the impedance mismatch region to C_{stray} .

3.2 The electrostatic analysis

One of the most important goals of this work is to determine the tolerance of the pickup installment. Due to mechanical constraints, pickups could be misaligned inside the BPM flange during the manufacturing process. Tolerance values need to be established for best BPM performance. CST Electrostatic Suite is used for all electrostatic parameter simulations.

Electrostatic simulation model is described by a single flange, where pickups are located. Figure 3.2 (a) demonstrates the vacuum flange with floating round disks for pickups. The difference in potential between a single pickup and the flange, allows the calculation of the capacitance to be made. As any numerical simulation software CST Electrostatic Suite heavily relies on boundary conditions, in which the model is set [19].

The flange is fairly short; and if boundary conditions are not setup correctly, fringing fields will affect simulation results. In order to eliminate fringing fields, the boundary condition are set tangential to Electric field E , Magnetic field H and current density J to simulate a very long beamline as shown in Figure 3.2 (b). Figure 3.2 (c)

demonstrates electric field orthogonal to the surface of the inner conductor, which indicates no fringing fields at the model edges.

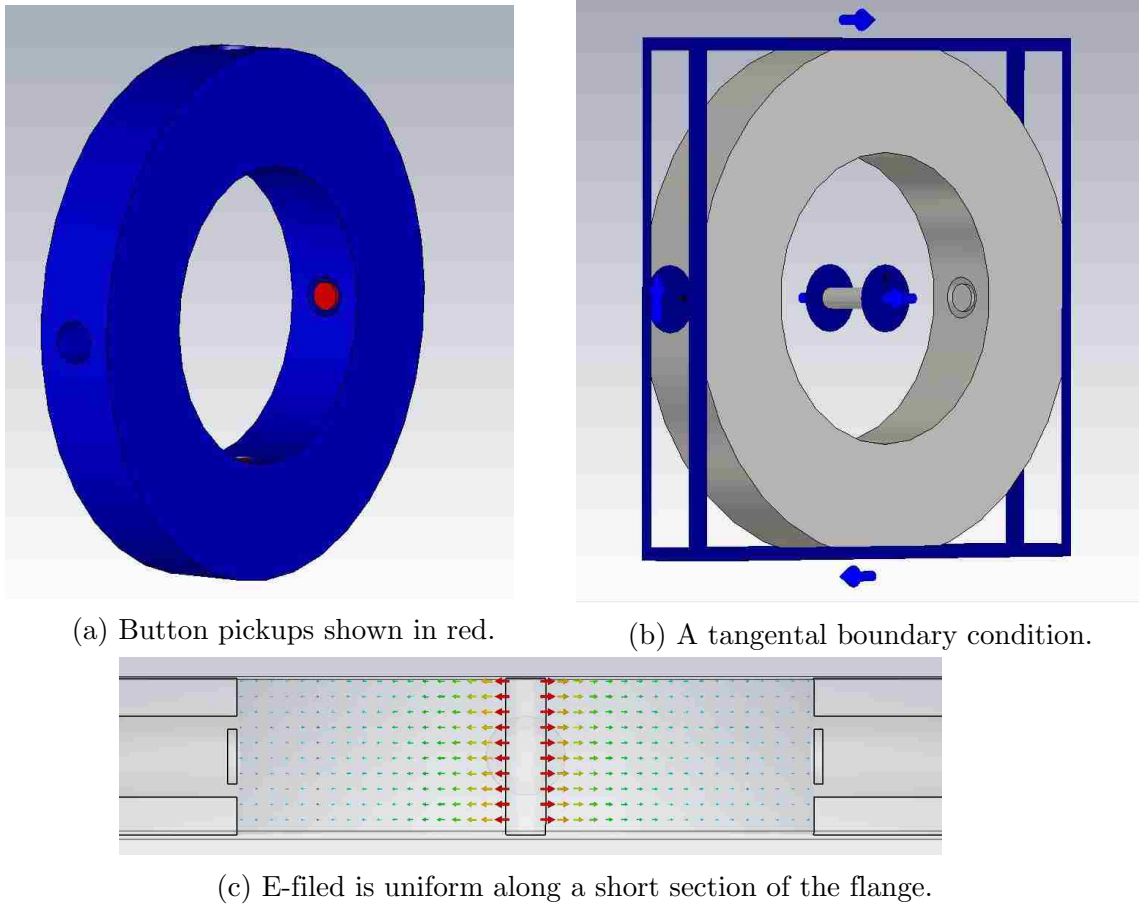


Figure 3.2: Boundary conditions demonstration for electrostatic simulations.

3.2.1 Electrostatic simulation of C_{stray} and C_{pickup} for a pickup disk

Section 2.5.2 shows an analytical calculation of capacitance values for C_{stray} and C_{pickup} of a pickup disk inside the BPM flange. Values were approximated to be $C_{stray}(analytical) = 121 \text{ fF}$ and $C_{pickup}(analytical) = 3.1 \text{ fF}$; however, due to these

approximations, the final capacitance values might not accurately represent the real capacitance of a pickup. To calculate capacitance values accurately, an electrostatic simulation is configured as shown in Figure 3.3. The electric field lines are noticeably focused on sharp edges of the disk, are called fringing fields [20]. Fringing fields lead to a nonlinear increase in the capacitance values calculations.

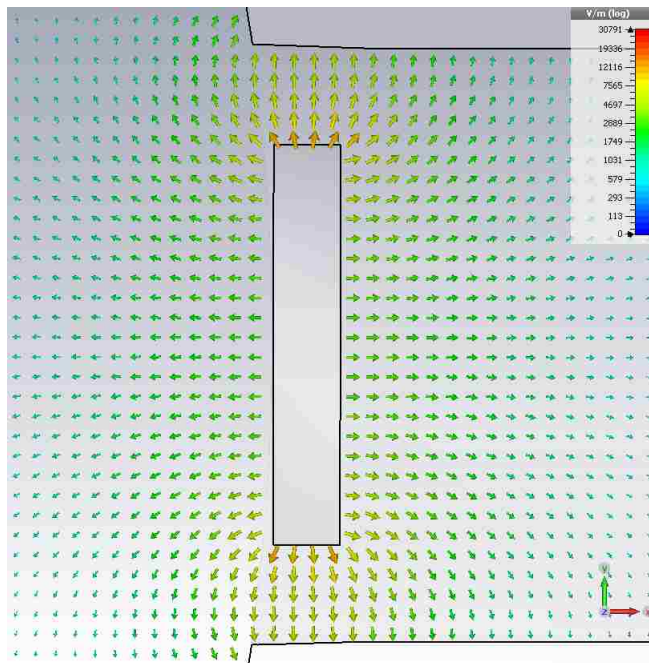


Figure 3.3: A pickup disk in the BPM flange.

The simulation calculated capacitance results to be $C_{stray}(simulated) = 488 \text{ fF}$ and $C_{pickup}(simulated) = 4.34 \text{ fF}$. The comparison between analytical and simulated capacitance values shows a significant increase in C_{stray} by 400%. The value of C_{pickup} was increased by about 18%. The accuracy of the electrostatic capacitance simulation was verified by decreasing the mesh size and increasing the number of iterations for each calculation, until results converged.

3.2.2 Displacement analysis of a pickup with a stem

The next step of the electrostatic simulation is to perform the analysis of the possible pickup displacements inside the flange. As discussed in the introduction of the following chapter the pickup is connected to the SMA feedthrough via a stem, which contributes to the total value of C_{stray} . The simulation was set in 4 possible beam positions as shown in Figure 3.4

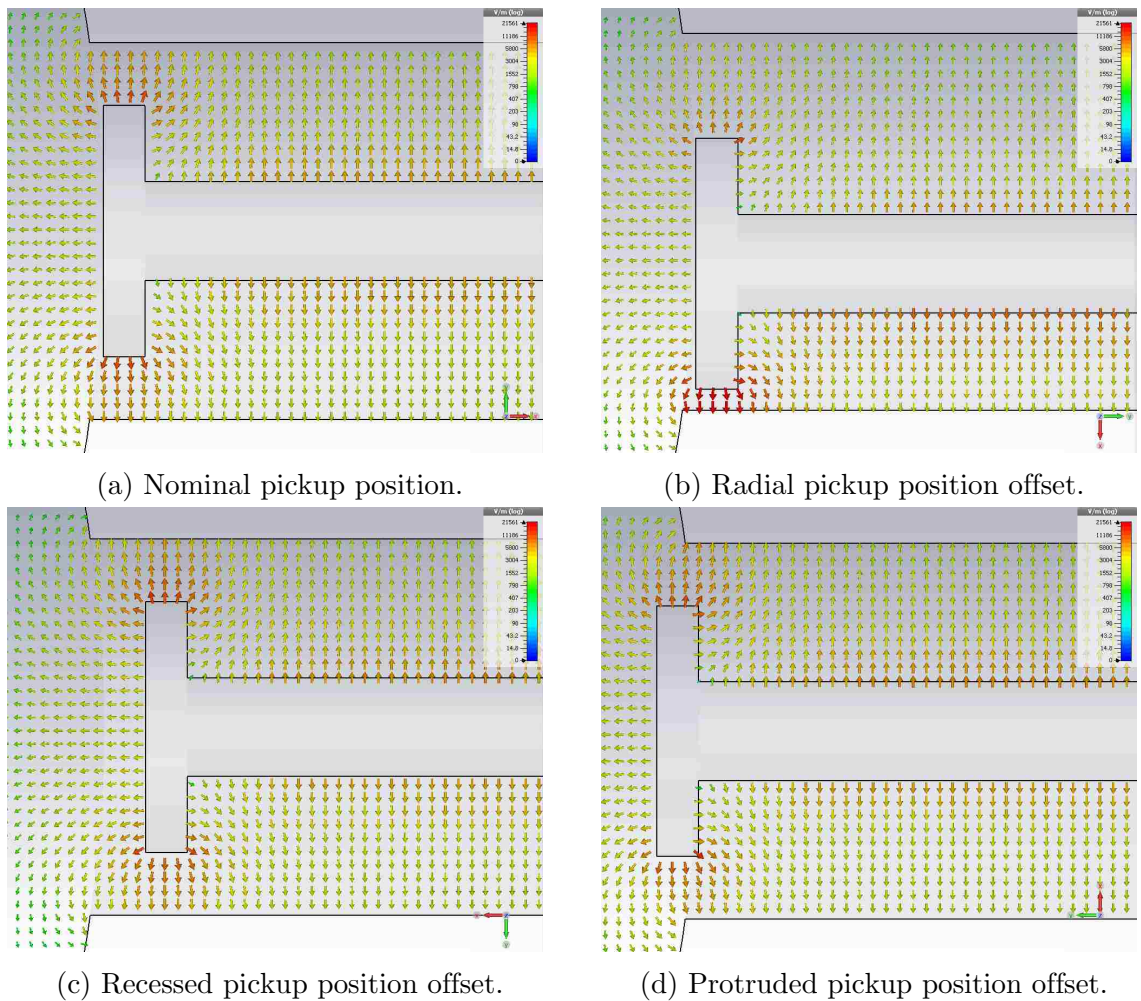


Figure 3.4: Pickup positions in the flange.(a)no displacement,(b) radial displacement, (c) recessed displacement,(d) protruded displacement. The displacements of pickups is 1 mm.

Chapter 3. Numerical analysis

The displacement on all figure(b),(c), and (d) equal to 1mm and the corresponding capacitance values are:

$$C_{stray} = 773 * 10^{-15} F \text{ (Nominal position)}$$

$$C_{stray} = 863 * 10^{-15} F \text{ (Radial displacement)}$$

$$C_{stray} = 780 * 10^{-15} F \text{ (Recessed displacement)}$$

$$C_{stray} = 754 * 10^{-15} F \text{ (Protruded displacement)}$$

A displacement of 1mm from the nominal position has a large deviation in C_{stray} ; therefore, a parameter sweep needs to be performed to study changes in C_{stray} as a function of radial displacement as shown in Figure 3.5. The x-axis shows the pickup radial displacement d_r and the y-axis shows the change in C_{stray} with respect to the nominal position in percent. d_r is varied from $d_r = 0 \text{ mm}$ (Nominal position) to $d_r = 1.3 \text{ mm}$ (the maximum radial displacement of the pickup) in increments of $100 \mu\text{m}$.

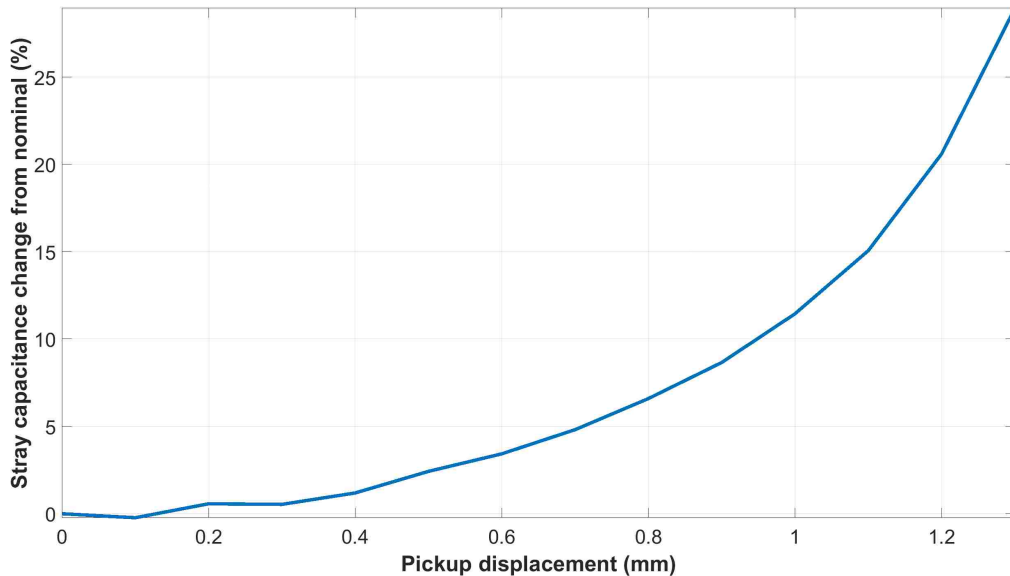


Figure 3.5: Change in stray capacitance as a function of radial pickup displacement.

Chapter 3. Numerical analysis

For the displacement up to $d_r = 0.2 \text{ mm}$, C_{stray} has a change of about 1%. Between $d_r = 0.2 \text{ mm}$ and $d_r = 0.6 \text{ mm}$ value for C_{stray} increases to about 4%. Passed $d_r = 0.7 \text{ mm}$ the change in C_{stray} increases exponentially. At the displacement $d_r = 1 \text{ mm}$, the capacitance value increased by about 12%.

In order to study the change in C_{stray} as a function of recessed and protruded displacements d_l a second parameter sweep is performed and the result is shown in Figure 3.6. The x-axis shows the change in longitudinal displacement, where $d_l = [-1.5; 0)$ is the protruded displacement towards the beam, $d_l = (0; 1.5]$ is recessed displacement away from the beam and $d_l = 0$ is the nominal displacement. The y-axis shows the change in C_{stray} with respect to the nominal position in percent.

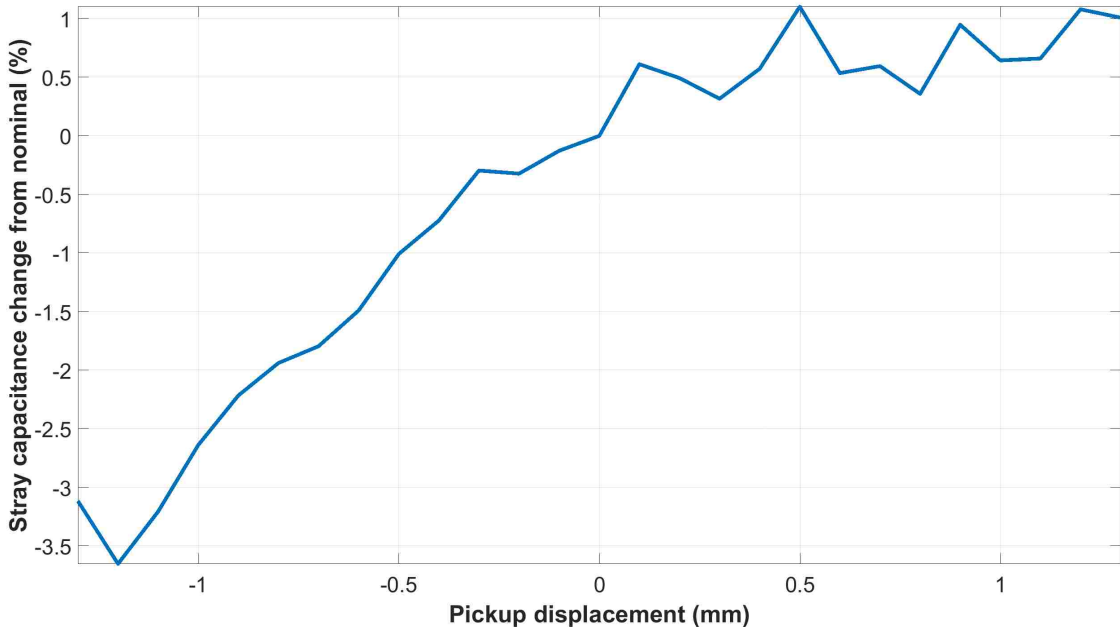


Figure 3.6: Change in stray capacitance as a function of pickup recessed and protruded displacement.

Figure above demonstrates the change in C_{stray} as a function of pickup displacement

Chapter 3. Numerical analysis

d_l . The value of C_{stray} changes very slightly as a function of longitudinal displacement, because C_{stray} is composed of the pickup disk stray capacitance and the stem capacitance. The stem capacitance makes up more than a half of C_{stray} and therefore the pickup disk displacement longitudinally changes the value for C_{stray} by less than 4 %.

The next capacitance value, in need of the simulation verification, is C_{pickup} . The simulation of C_{pickup} in the nominal position yields the result

$C_{pickup} = 4.34 * 10^{-15} F$ and, according to the same nomenclature defined in Figure 3.4, values for C_{pickup} were simulated for each displacement:

$$C_{pickup} = 4.34 * 10^{-15} F \text{ (Nominal position)}$$

$$C_{pickup} = 4.22 * 10^{-15} F \text{ (Radial displacement)}$$

$$C_{pickup} = 2.55 * 10^{-15} F \text{ (Recessed displacement)}$$

$$C_{pickup} = 6.74 * 10^{-15} F \text{ (Protruded displacement)}$$

As expected, the radial displacement does not affect C_{pickup} as drastically as the pickup displacement closer and further from the beam. To determine the behavior of C_{pickup} as a function of longitudinal displacement a parameter sweep needs to be performed.

Similarly to Section 2.5.2, the radius of the beam is set to be $r_{beam} = 2.35 \text{ mm}$. The position of the beam remained centered in the flange and the position of the pickup varied from $d_l = [-1.5, 1.5] \text{ mm}$ as shown in Figure 3.7. The x-axis shows the change in longitudinal displacement, where $d_l = [-1.5; 0)$ is the protruded displacement towards the beam, $d_l = (0; 1.5]$ is recessed displacement away from the beam and $d_l = 0$ is the nominal displacement. The y-axis shows the change in C_{pickup} with respect to the nominal position in percent.

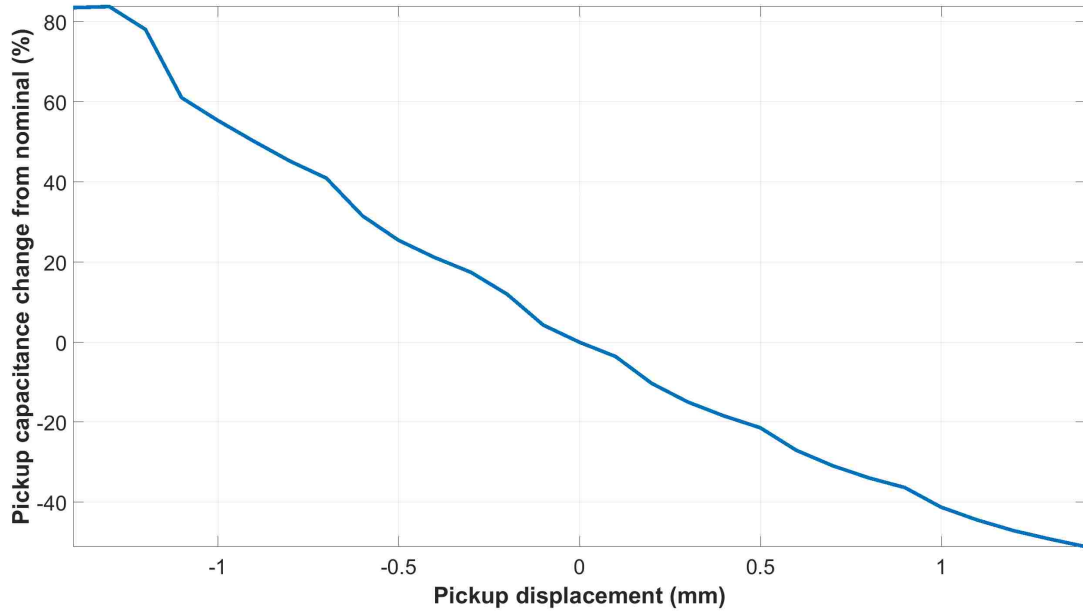


Figure 3.7: Change in pickup capacitance as a function of recessed and protruded displacement.

The difference between C_{pickup} values at end points of d_z varies significantly. When the pickup is protruded to $d_l = 1.5[mm]$, C_{pickup} value increases by 90%, which can drastically influence the BPM measurements.

3.3 SPICE simulation

Chapter 2 discussed the new idea of modeling the BPM system represented as a simple equivalent circuit, as shown in Figure 3.8. The circuit depends only on three variables: C_{stray} - the parasitic capacitance between the pickup and the flange, C_{pickup} - the capacitive couple between the beam and the pickup and R_c the characteristic impedance of the transmission line connected to the pickup. Capacitance values for C_{pickup} and C_{stray} were calculated in the previous section.

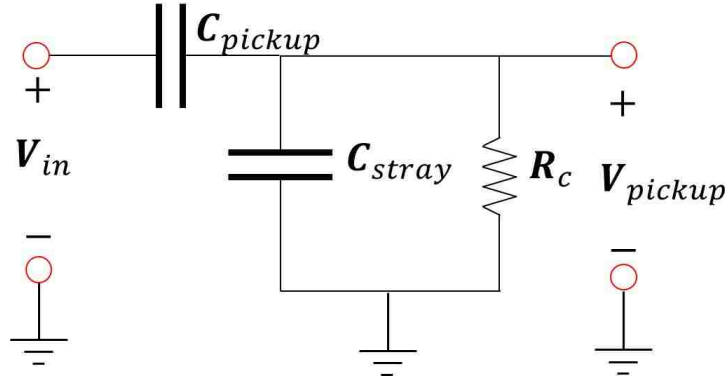


Figure 3.8: Simplified circuit for the BPM system.

A transfer function for above circuit was derived in Chapter 2 and could be expressed as the following equation

$$H(s) = \frac{V_{pickup}}{V_{in}} = \frac{sR_c C_{pickup}}{sR_c(C_{pickup} + C_{stray}) + 1} \quad (3.1)$$

The cutoff frequency for the transfer function can be expressed as equation 3.2

$$f_c = \frac{1}{2\pi R_c(C_{stray} + C_{pickup})} \quad (3.2)$$

Governed by equation 3.2, a cutoff frequency was calculated for each case described in Figure 3.4 and recorded in the table below

Table 3.1: Capacitance and calculated cutoff frequency results for 4 pickup position cases.

Case	C_{pickup} (fF)	C_{stray} (fF)	f_c (GHz)
Nominal pos.	4.34	773	4.1
Radial disp.	4.22	863	3.7
Recessed disp.	2.55	780	4.1
Protruded disp.	6.74	754	4.2

The SPICE software is now used in order to simulate transfer functions for each

Chapter 3. Numerical analysis

pickup displacement case. Capacitance values for C_{pickup} and C_{stray} from Table 3.1 were used to simulate transfer functions in SPICE for each displacement case.

The SPICE simulation frequency range was set 100 MHz to 100 GHz to demonstrate the asymptotic value of the transfer function. Figure 3.9 demonstrates simulated results of transfer functions. Solid lines represents the absolute magnitude of transfer functions in dB and correspond to left y-axis label. Dashed lines represent the phase of transfer functions in degrees and correspond to the right y-axis label.

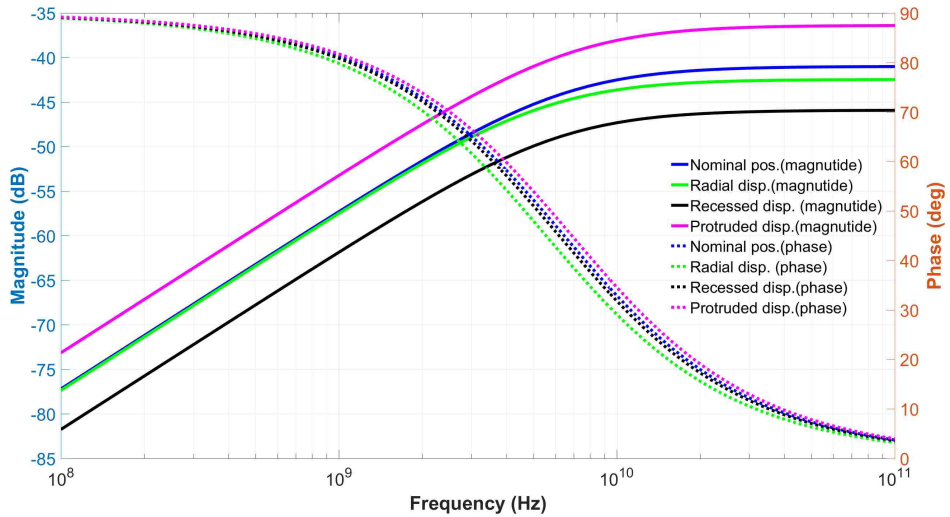


Figure 3.9: SPICE simulation of transfer functions for 4 pickup positions. Solid lines are magnitude values, dashed lines are phase values

Notice the difference transfer functions based on the pickup position. Radial displacement does not affect the position of the transfer function much, yet affects the cutoff frequency as shown in Table 3.1. The protruded displacement of the pickup increases the C_{pickup} , which shifts the transfer function to a higher magnitude. The recessed displacement reduces C_{pickup} , which results in decreases the magnitude of the transfer function. When compared, the transfer function derived analytically and SPICE simulation of the circuit, results agree, which proves that the derivation was

done correctly.

3.4 Transfer function simulation for an infinite line BPM

Driven by results obtained from SPICE simulation, the microwave studio simulation was used to verify results. A short section of an infinitely long beamline was modeled in Microwave Studio [21]. Figure 3.10 demonstrates the geometry of the beamline model. Red squares define perfectly matched waveguide ports as an ideal wave source and an ideal wave sink. There is no reflection between waveguide ports, which results in an infinite electrical length of the beamline. The interaction space between waveguide ports includes the BPM with 4 pickups located 90 degrees offset from each other.

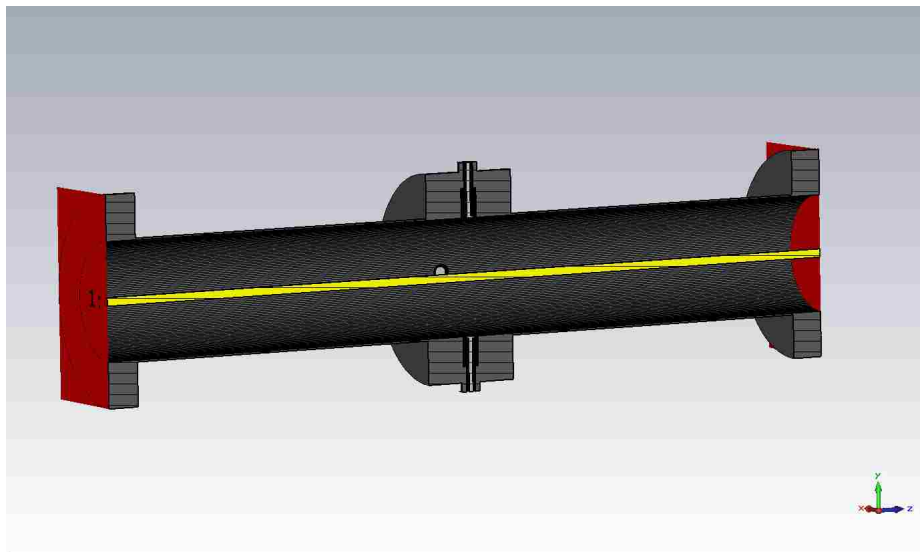


Figure 3.10: A cross section of section for an infinitely long beamline.

Chapter 3. Numerical analysis

As mentioned in Section 3.1 the button is connected to the SMA feedthrough via a short stem. The impedance mismatch is recreated with an appropriate impedance regions as shown in Figure 3.11.

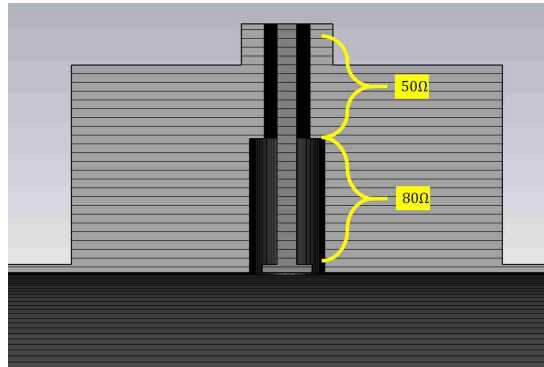


Figure 3.11: Nominal position of a BPM pickup connected to a stub.

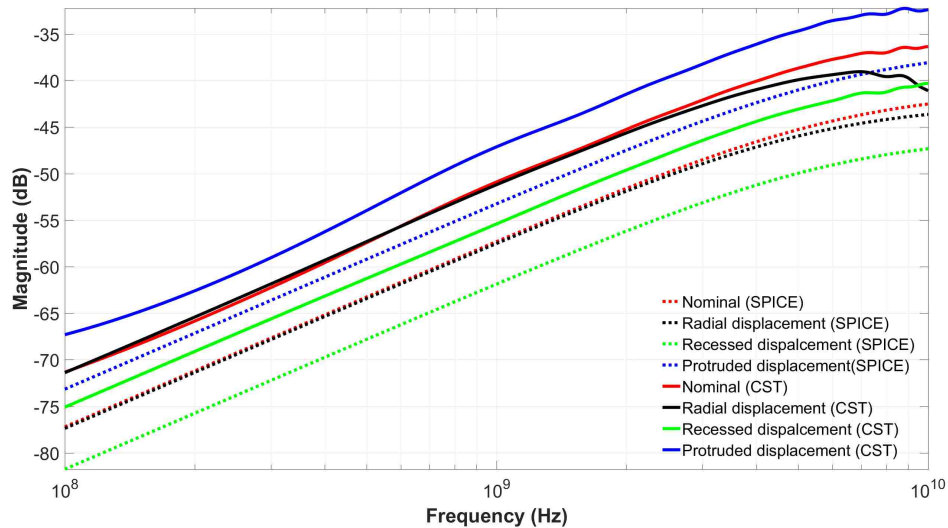


Figure 3.12: Transfer function result comparison of SPICE simulation vs CST simulation.

The comparison of Microwave studio and SPICE results for each displacement case

is shown in Figure 3.12. The transfer functions are plotted in the range [100 MHz, 10 GHz]. By observation, both, SPICE and Microwave Studio results have similar signal shapes and also the same cutoff frequencies; however the amplitude of transfer functions was not the same. All correlating transfer functions are offset by about 5dB.

The nature of the amplitude difference is unclear and through multiple manipulation of variables and repeated simulations the difference remained the same. It is believed that the difference is caused by a numerical simulation artifact. Despite a small amplitude variation, the numerical simulation model fully supports the analytical circuit model, which means, the BPM can be characterized using a transfer function.

3.5 Frequency domain model of an experimental setup for BPM characterization test stand

A transfer function from the circuit model proves to be working for characterizing the BPM system. An experimental set up was designed; however prior to taking the experimental data a numerical simulation needs to be done to understand a complicated geometry of the experimental setup and effects the geometry could have on experimental results of the transfer function. The work flow demonstrates step-by-step progression of increasing geometry complications, from a simple coaxial transmission line to a complete experimental.

The frequency range for all simulation is [100MHz,10GHz]. The following names are used for all steps:

- R_o The radius of the outer conductor
- R_i The radius of the inner conductor

- L The length of the coaxial line.
- R_b The radius of the beam
- $L(\text{port})$ The length of the Port.

3.5.1 Case A. The ideal coaxial transmission line of length L

The first and simplest case used is an ideal coaxial transmission line of length L . The length of the transmission line in this case is $L = 100 \text{ mm}$. The ratio of $R_o = 1.5 \text{ mm}$ to $R_i = 0.65 \text{ mm}$ is chosen to be such, that the characteristic impedance of the coaxial line results to be 50 Ohm.

The simulation is set for Port 1 and Port 2 to match the impedance of the coaxial line on each side. Only the fundamental mode is considered. The mode is expected to be TEM mode due to the coaxial geometry [22].

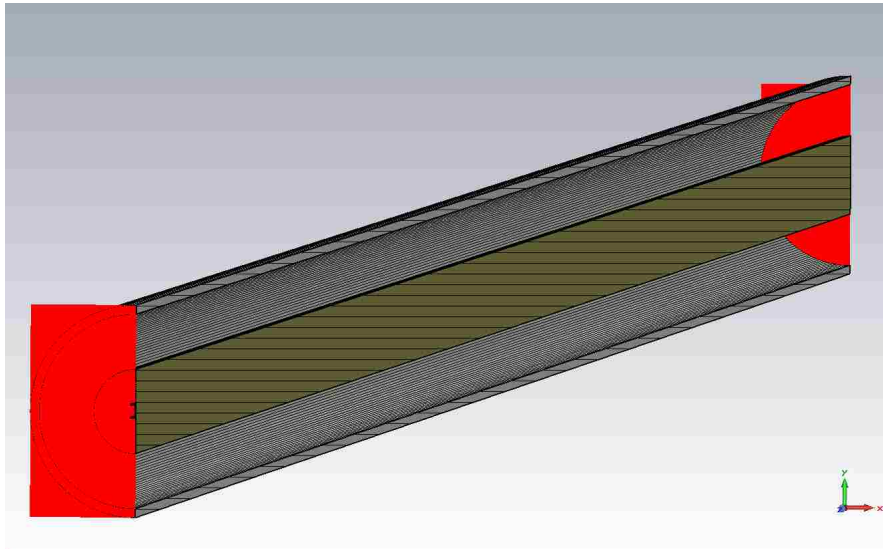


Figure 3.13: Case A. Coaxial transmission line with characteristic impedance of 50 Ohm.

S_{21} measures transmission of the energy from port 1 to Port 2. The measurement S_{21} is expected to be very close to zero due to no reflections or losses. S_{11} measures the reflection of energy transmitted from port 1. The S_{11} measurement is expected to have a very large negative number measured in dB. Figure 3.14 demonstrates S-parameter results as predicted.

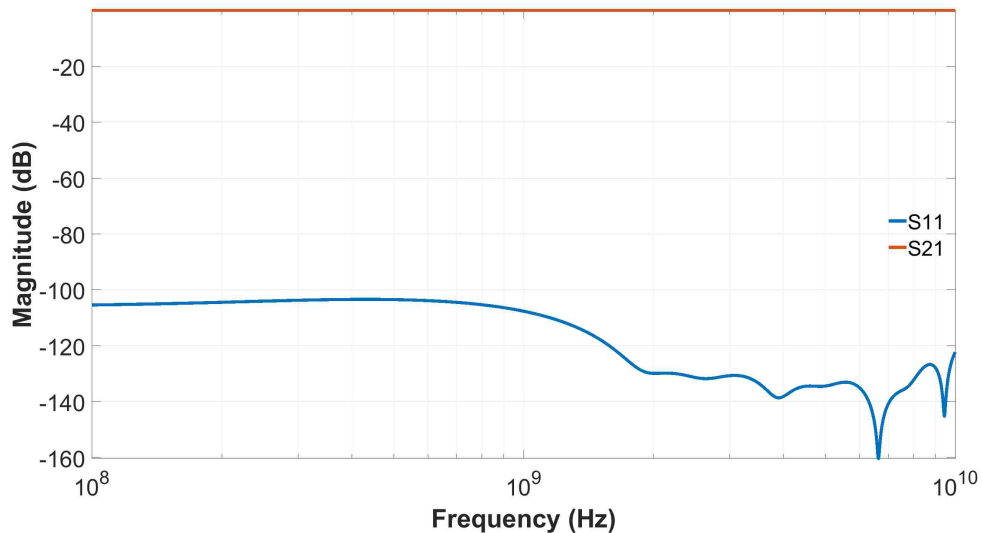


Figure 3.14: Case A S-parameters for the coaxial transmission line with characteristic impedance of 50 Ohm.

3.5.2 Case B. The ideal coaxial transmission line with an impedance mismatch section

As a first alteration to the transmission line, the outer conductor radius is changed to $R_o(right) = 8.85mm$. The change in radius introduces the region of the impedance mismatch as shown in Figure 3.15.

$$L = 100mm$$

Chapter 3. Numerical analysis

$$R_i(left) = 0.655mm \quad R_o(left) = 1.5mm$$

$$R_i(right) = 0.655mm \quad R_o(right) = 8.85mm.$$

The characteristic impedance $Z_c(left) = 50\Omega$, $Z_c(right) = 233\Omega$

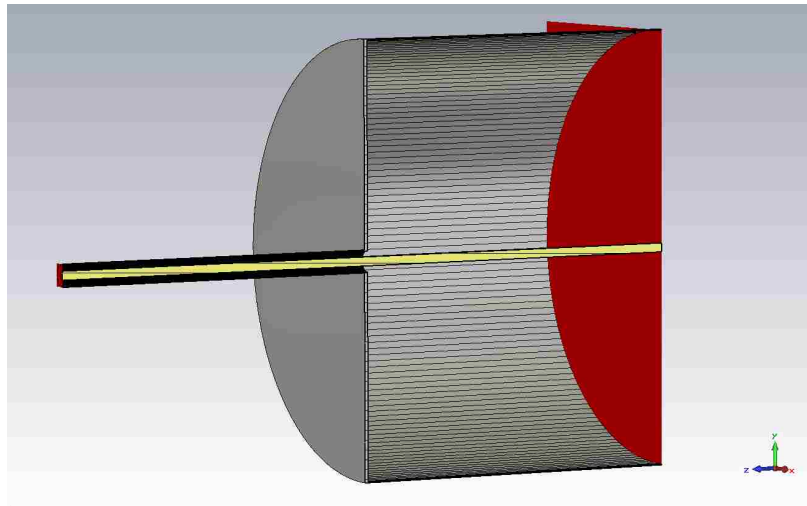


Figure 3.15: Case B. A transmission line two different impedance values.

Figure 3.16 demonstrates a different behavior of S-parameters than in Case A. The plot can be explained in two parts: on the interval [100 MHz,4 GHz] and [4 GHz,10 GHz].

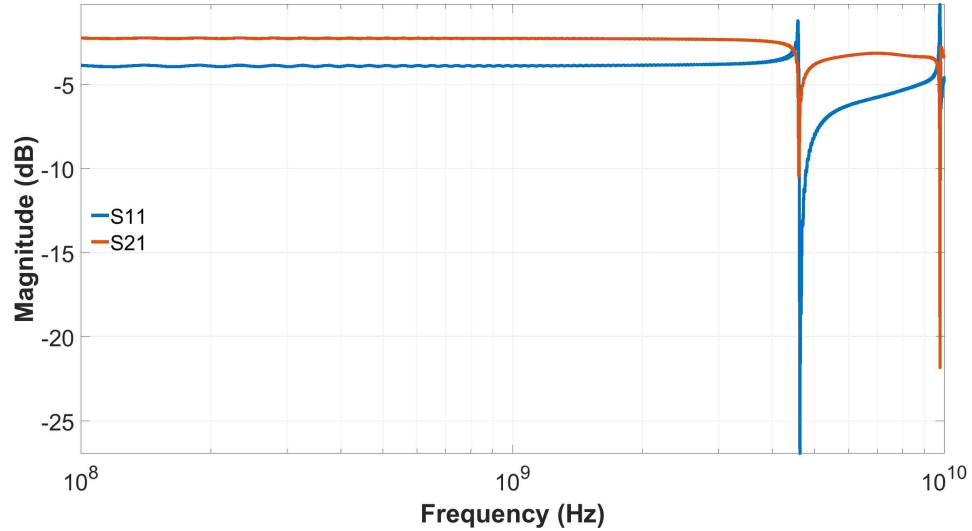


Figure 3.16: Case B. S-parameters for a coaxial line with two different characteristic impedance sections.

At a lower frequency range up to 4 GHz, S_{11} is no longer large negative value, instead S_{21} is close to -2 dB, and S_{11} is close to -4 dB. This behavior could be explained with impedance mismatch. In the current simulation Port 1 and Port 2 are perfectly matched, however the structure in the middle creates an interface of impedance mismatch. The reflection coefficient Γ is defined according to the following equation

$$\Gamma = \frac{Z_{right} - Z_{left}}{Z_{right} + Z_{left}} \quad (3.3)$$

Given characteristic impedances at each port the value of Γ is calculated to be 0.647 or -3.78 dB. The simulation results for S_{21} and S_{11} are well supported by the impedance mismatch analysis.

At the frequency range above 4 GHz the behavior of S_{21} and S_{11} is slightly different. Two major dips could be seen at $f_1 = 4.62GHz$ and $f_2 = 9.78GHz$. Notice that at $f_1 = 4.62GHz$ both S_{21} and S_{11} have a dip. The following behavior concludes,

higher order modes propagating inside of the transmission line, which allows the power to be transmitted at this frequency. The simulation for Case B needs to be repeated; however, 5 first modes are calculated at Port 2. The visualization of ports are shown in Figure 3.18.

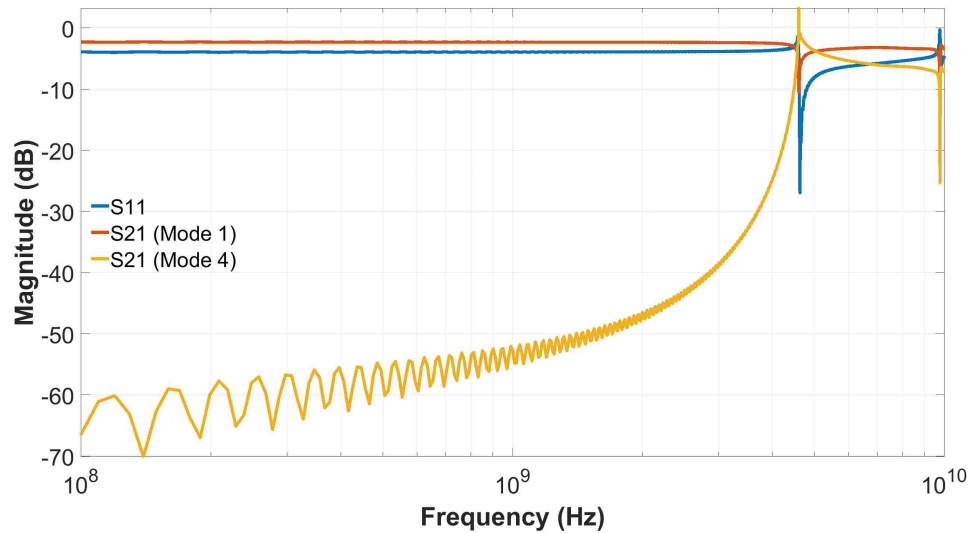


Figure 3.17: Case B. S-parameters results for S_{11} , S_{21} (fundamental mode) S_{21} (mode 4).

An observation can be made, that the fundamental mode S_{21} (Mode 1) accounts for the majority of the signal transmission as expected, while other modes have very large negative value in dB. The contribution from most modes is negligible except for fourth mode S_{21} (Mode 4). The following mode does not transmit nearly any power up to 4 GHz and at 4.6 GHz the majority of the signal is transmitted through Mode 4. Remaining modes are not shown in the figure, because their magnitudes are below -100 dB value and they do not contribute to the signal transmission.

Cutoff frequencies for circular waveguide modes are calculated with a help of Bessel function roots [22]. The cutoff frequency of the given TE mode is calculated using Equation 3.4

$$f_{c_{nm}}(TE) = \frac{p'_{nm}c}{2\pi R_0\sqrt{\mu_r\epsilon_r}} \quad (3.4)$$

Where R_0 is the radius of the circular waveguide and p'_{nm} is given in Table 3.2

Table 3.2: Values of p'_{nm} for TE modes of a Circular waveguide

n	p'_{n1}	p'_{n2}	p'_{n3}
0	3.832	7.016	10.174
1	1.841	5.331	8.536
2	3.054	6.706	9.970

Similarly the cutoff frequency for TM modes can be calculated using equation 3.5.

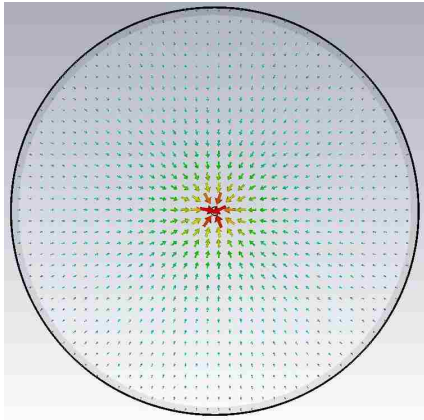
p_{nm} values are used from Table 3.3 [22]

$$f_{c_{nm}}(TM) = \frac{p_{nm}c}{2\pi R_0\sqrt{\mu_r\epsilon_r}} \quad (3.5)$$

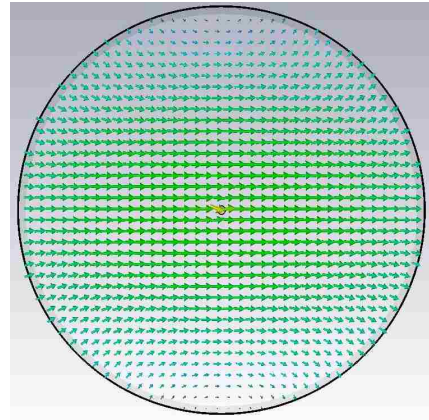
Table 3.3: Values of p_{nm} for TM modes of a Circular waveguide

n	p_{n1}	p_{n2}	p_{n3}
0	2.405	5.520	8.654
1	3.832	7.016	10.174
2	5.135	8.417	11.620

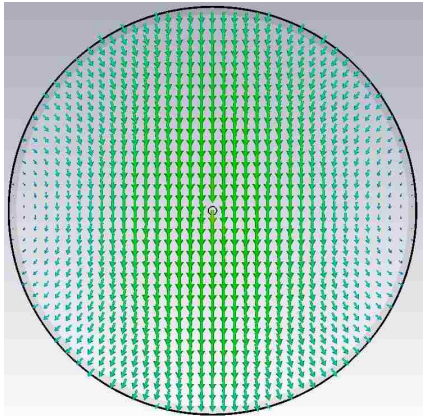
By calculating cutoff frequency for these modes, results are very accurate for TE modes and values could be seen at Figure 3.18, however for the mode of interest TM01 results vary. $f_{c_{01}}(\text{calculated}) = 3.6GHz$, while CST calculate the result to be $f_{c_{01}}(CST) = 4.34GHz$.



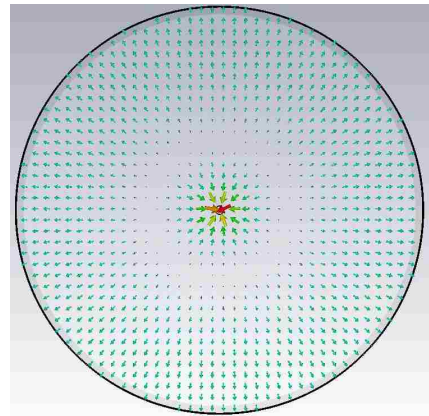
(a) Fundamental mode TEM.



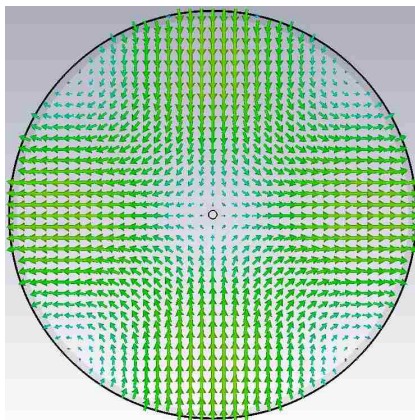
(b) Mode 2 TE11 $f_c = 2.76 \text{ GHz}$.



(c) Mode 3 TE11 $f_c = 2.76 \text{ GHz}$.



(d) Mode 4 TM01 $f_c = 4.59 \text{ GHz}$.



(e) Mode 5 TE21 $f_c = 4.59 \text{ GHz}$.

Figure 3.18: Port 2 mode visualization with simulated cutoff frequencies.

Provided results suggest that the ratio between inner and outer conductors is

Chapter 3. Numerical analysis

so large, that the cavity acts as a cylindrical wave guide, rather than a coaxial waveguide, allowing higher order modes to be propagated. In the coaxial transmission line the fundamental mode is TEM and higher order modes are suppressed by the presence of the inner conductor in the cylindrical cavity[23].

It is important to identify why higher order modes are being excited. The coaxial transmission line transmits the signal when the inner conductor is excited with voltage. The real signal, traveling on the inner conductor of the TL, induces an image signal on the surface of the outer conductor. Both signals are traveling along the TL, however, the length of these paths can be different. Consider an example demonstrated in Figure 3.19.

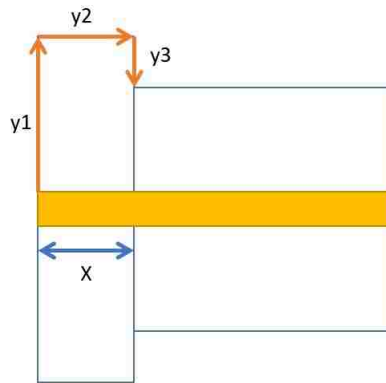


Figure 3.19: Path difference of real signal vs image signal concept.

Y is the total path of the image signal on the surface of the outer conductor, where $Y = y_1 + y_2 + y_3$. X is the total path of the real signal on the surface of the inner conductor, where $X = x$. The difference between these paths introduces the phase shift between these signals. If $Y - X = \frac{\lambda}{2}$, the transmission could go to zero due to the destructive interference.

Chapter 3. Numerical analysis

For Case B, $Y - X = 32.4mm$, which corresponds to a destructive interference to occur at around 4.6 GHz. The peak is well supported by simulated results and above analysis. Case B is critical in all future steps, because it lays the foundation of the further analysis understanding, .

The final function for Case B is to define the notion of the "SMA port", which is used in further cases. A real SMA port is used in the experimental setup; therefore, the SMA port influence needs to be modeled in the simulation. Figure 3.15 demonstrates the two parts of the transmission lines with different radii of the outer conductor. The length of the section on the left could be reduced to $L(port) = 5mm$.

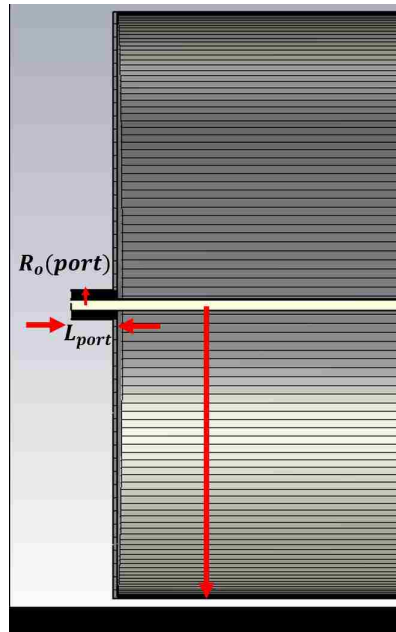


Figure 3.20: 50 Ohm port closeup.

The change in length for the excitation port (shown above) does not affect results for dips, similar to SMA ports in real systems.

3.5.3 Case C. 156 Ohm coaxial transmission line with 50 Ohm SMA port

Case B demonstrated the behavior of the system as the result of a beamline cavity acting as a cylindrical waveguide and a half wavelength resonator. The change applied in Case C is the interface between inner conductors.

$$L(port) = 5mm, L(beamline) = 100mm$$

$$R_i(port) = 0.655mm \quad R_o(port) = 1.5mm$$

$$R_b(Beamline) = 2.35mm \quad R_o(Beamline) = 31.755mm.$$

The characteristic impedance $Z_c(port) = 50\Omega$, $Z_c(Beamline) = 156\Omega$

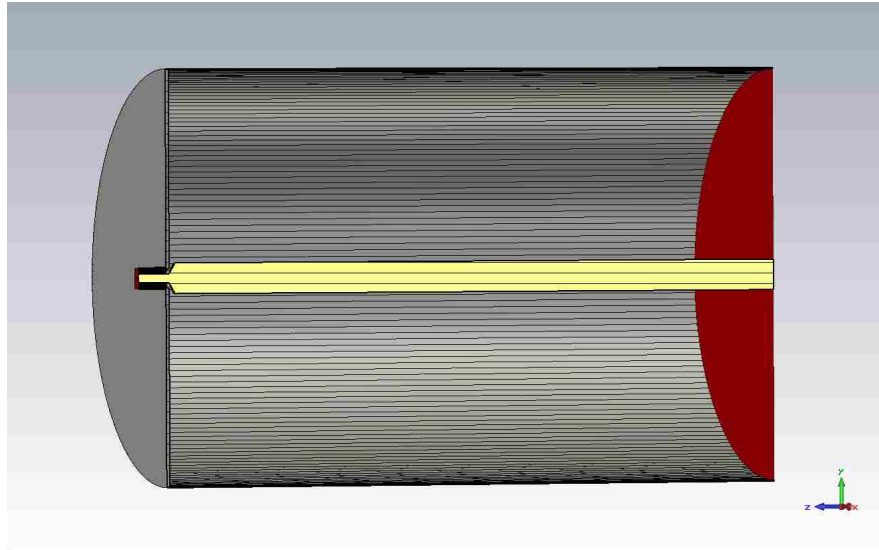


Figure 3.21: Case C. 156 Ohm Beamline with SMA port.

Notice a smooth transition between $R_i(port)$ to R_b with a solid cone. Prior to this setup, the interface did not include the smooth transition, resulting in spikes in S_{21} . In order to eliminate spikes, a conical transition was used to join $R_i(port)$ and R_b .

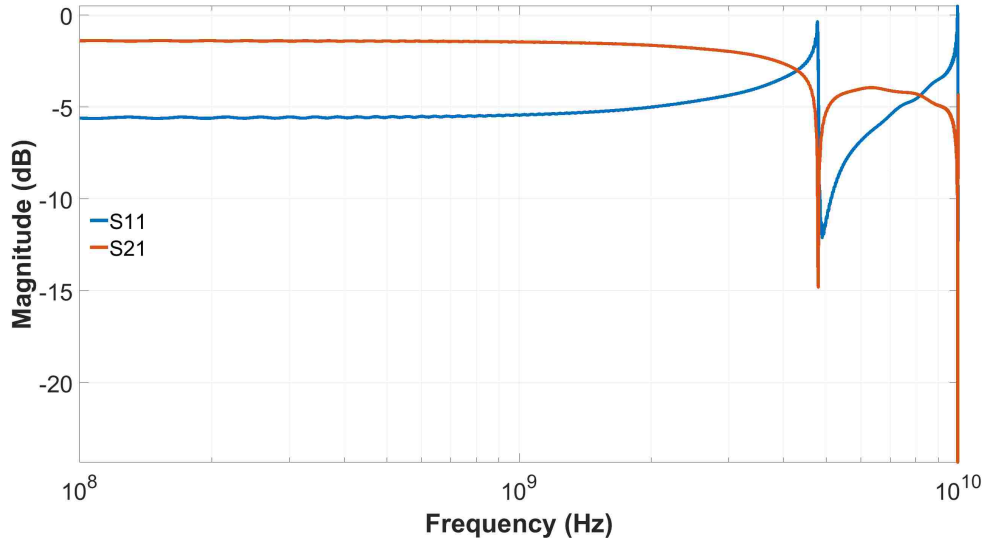


Figure 3.22: Case C.S-Parameters for 156 Ohm Coaxial transmission line with 50 Ohm SMA port.

Figure 3.22 demonstrates the behavior of S_{21} and S_{11} similar to Case B. Only with one difference. Since R_b was increased, the ratio between inner and outer conductor was decreased. The lower order mode is suppressed and the dip at $f_1 = 4.8GHz$ is due to 6th mode. In the current case $Y - X = 31.12mm$, which is predicts the dip to occur at $4.82GHz$. Mode analysis also showed that the 6th mode of at Port 2 is TM_{01} mode. A conclusion could be made that in a coaxial line, the inner conductor suppresses lower order TE modes, however interact with TM_{01} mode.

3.5.4 Case D. The 156 Ohm line terminated with SMA ports at each end

The last step that needs to be address is the termination of both sides of the Beamline with SMA ports. So far all simulations were done with a single SMA port at Port 1 and Port 2 was matched waveguide port impedance. Figure 3.23 demonstrates the simulation setup with the following parameters:

Chapter 3. Numerical analysis

$$L(\text{port}) = 5\text{mm} \quad L(\text{beamline}) = 100\text{mm}$$

$$R_i(\text{SMA port}) = 0.655\text{mm} \quad R_o(\text{port}) = 1.5\text{mm}$$

$$R_b(\text{Beamline}) = 2.35\text{mm} \quad R_o(\text{Beamline}) = 31.755\text{mm}.$$

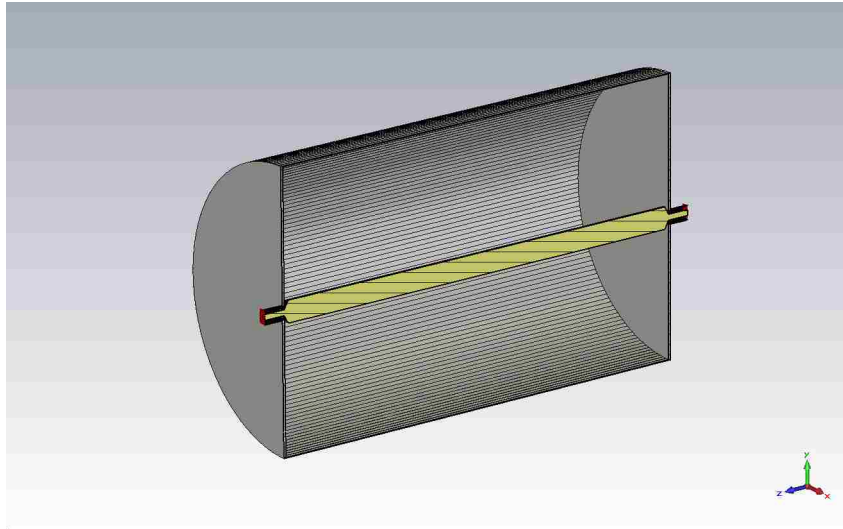


Figure 3.23: Case D geometry. The beamline is terminated at both ends with SMA ports.

Figure 3.24 shows S-parameter behavior of the system. Standing waves could be observed in the structure. The presence of standing waves is expected in this situation, because a coaxial structure is bound by two interfaces with mismatched impedances.

As shown in previous cases, impedance mismatch interface can cause the signal to be reflected. In a system with multiple mismatching points, multiple reflections could occur. Based on reflected signals standing wave would no longer propagate in the system, but rather oscillate. Equation 3.6 demonstrate the wavelength for the given length of the waveguide.

$$\lambda_n = \frac{2}{n}L \rightarrow f_n = \frac{\nu n}{2L} \quad (3.6)$$

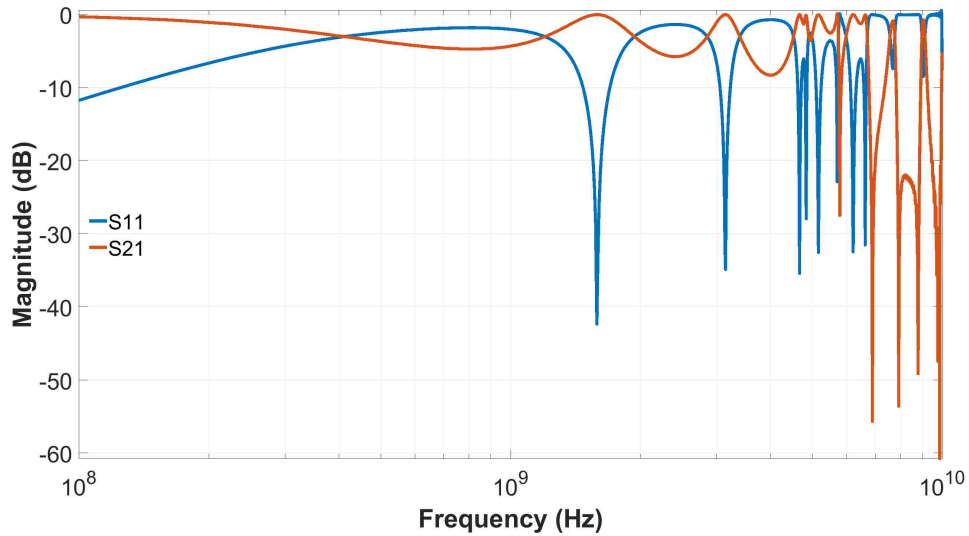


Figure 3.24: Case D S-Parameters. Standing waves could be observed.

The length of the main beamline is $L(\text{beam}) = 100\text{mm}$. Based on Equation 3.6 standing waves are expected at $f_r = 1.5\text{GHz}$ and the integer multiples of the resonant frequency. The calculation is well supported by simulations. At higher frequencies it could be noticed, that higher order modes interact with standing waves resulting in the pattern shown on Figure 3.24.

3.5.5 Case E. A complete BPM setup

Cases A-D demonstrated basic principles of signal behavior in the system. Cases E and Case F demonstrate the complete experimental test bed including dimensions for Vacuum tubes, conflat connections and Beam Position Monitor flange. There are several goals of interest:

Chapter 3. Numerical analysis

- Minimize standing waves
- Minimize $Y - X$ effect
- Suppress higher order modes to reduce unwanted higher frequency behavior.

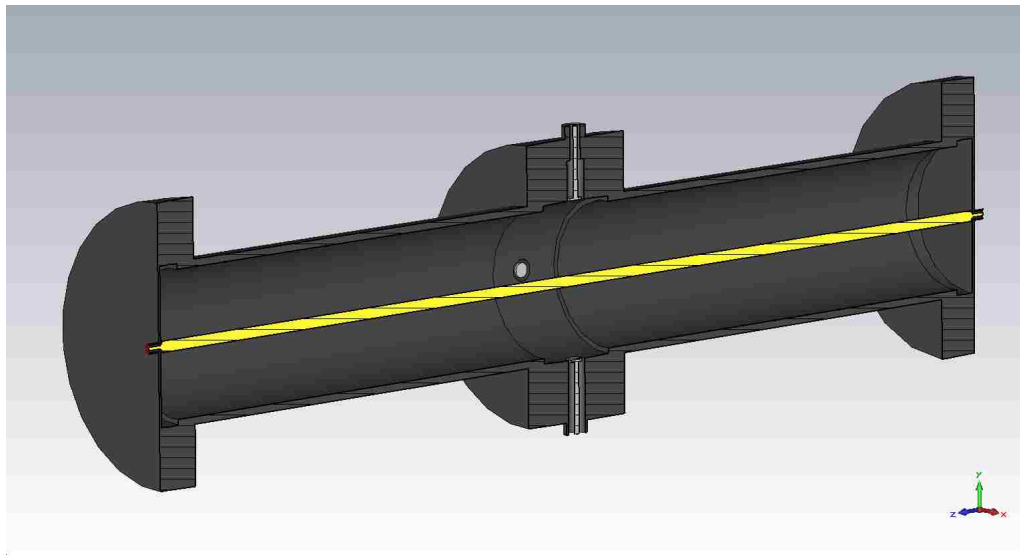


Figure 3.25: Case E Geometrical representation of BPM experimental setup.

That experimental setup needs both sides to have a measurement port. The inclusion of the measurement ports in the model is for better understanding the behavior of the physical system. It is impossible to perfectly terminate the large port in the experimental setting and the model needs to have two endplates with SMA ports connecting to them and denoted as Port 1 and Port 2. SMA ports play a role of measuring ports and will be important in the next chapter. A BPM flange is located in the middle of the structure and also terminated with 50 Ohm port and denoted as Port 3. The measurement of S_{31} provides the transfer function of the BPM in the experimental setting.

A calculation of $Y-X$ for Case E results to be approximately $Y - X = 28.3 \text{ mm}$. Based on these calculation the resonating frequency is expected at $f_{Y-X} = 5.3 \text{ GHz}$.

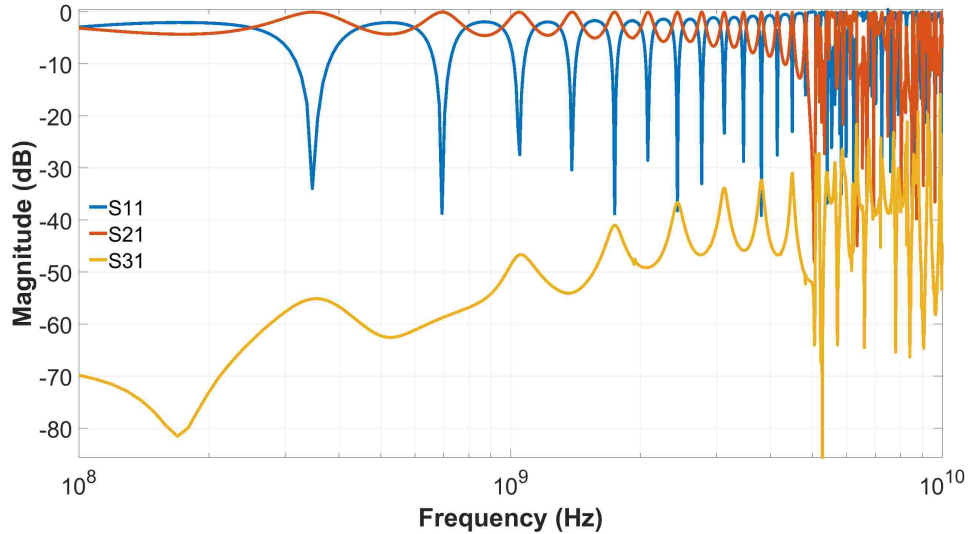


Figure 3.26: Case E S-parameters for S_{11} , S_{21} , S_{31} .

Figure 3.26 demonstrates results for S_{31} as well as S_{21} and S_{11} . Standing waves are present in the system correlating to the length of the model. Notice the number of peaks for S_{21} and S_{31} is different. Standing wave peaks are present only at frequencies that correlate to add integer multiples of the first standing wave. That behavior is caused by the location of the BPM flange in the model: in the middle. Peaks of standing waves for even integer multiples are symmetric and are not measured by pickups. Odd multiples, however, are well detected by the BPM.

The resonant frequency due to the $Y - X$ effect is present at $f_{Y-X} = 5.3 \text{ GHz}$, which is supported by S parameter measurements, specifically a dip is present at that frequency for S_{21} as well as S_{31} . In order to minimize $Y - X$ effect, increasing the resonant frequency out of the operating region a conical sections need to be used.

3.5.6 Case F. A complete BPM setup with conical reducers

In order to minimize $Y - X$ effects, two conical reducers are introduced in the system on both sides. Similarly to the previous case, conical reducers are terminated with metallic endplates with SMA ports connected to them. The following model mimics the configuration of the experimental setup with a high accuracy as shown in Figure 3.27. The following experimental configuration has a length path of $Y - X = 18.43 \text{ mm}$, which correlates to the resonant frequency at $f_{Y-X} = 8.14 \text{ GHz}$.

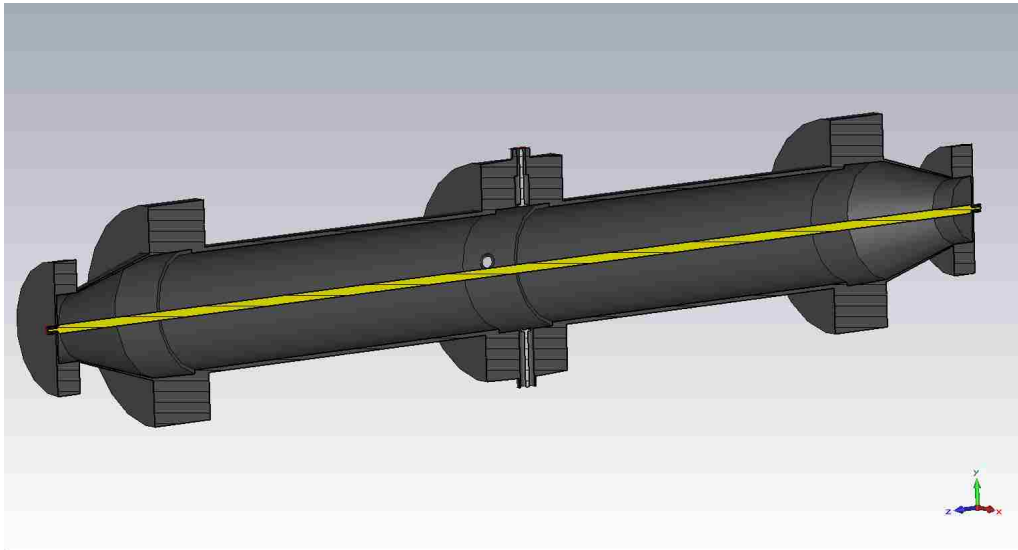


Figure 3.27: Case F Beamline with two conical reducers at each side.

Figure 3.28 S parameter results for Case F. Standing waves are present as in the previous case and they correspond to the length of the model. Similarly to Case E, standing waves measured by S_{31} are repeated for every other standing wave dip of S_{21} . $Y - X$ dip, present in the system, is supported by simulated results. The $Y - X$ analysis proved itself to be correct for the experimental model simulation. The introduction of conical reducers provides the reduction of $Y - X$, which increases the resonant frequency f_{Y-X} , out of operating frequency region.

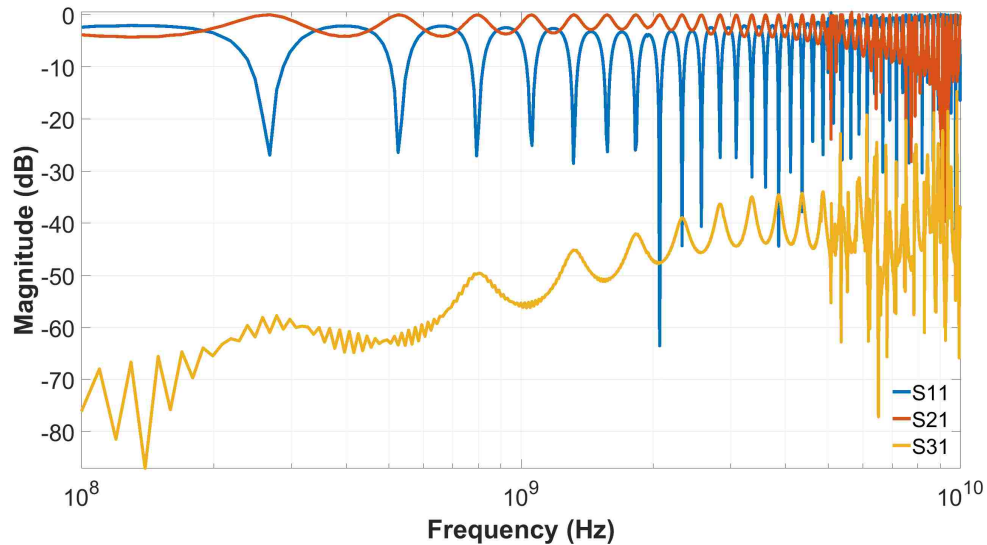


Figure 3.28: Case F S-Parameters for the BPM system with conical reducers at each side.

3.6 Conclusion

The goal of Chapter 3 was to continue the BPM characterization process, using numerical simulation codes. The circuit model provided a simple solution to a BPM characterization through a transfer function. A finite element time domain model was created to produce a transfer function. Time domain and SPICE transfer functions were compared to result in nearly full agreement. The shape and the cutoff frequency of both transfer functions were the same; however, there was a slight difference in magnitudes by about 5 dB. After multiple simulations under various parameters the difference in magnitude remained to be present. It appeared that the different was caused by a numerical simulation artifact. Despite the difference in magnitudes, the transfer function proved to be a reliable way for a BPM characterization. Along with the time domain of a perfectly matched beamline, a step-by-step derivation of the experimental test bed was developed. The experimental setup had multiple

Chapter 3. Numerical analysis

components with fine details, effects of which could affect the transfer function. The next chapter focuses on the experimental measurements of the transfer function.

Chapter 4

Experimental analysis

4.1 Introduction

Chapter 3 focused on the development of the numerical simulation model for the Beam Position Monitor. The following chapter focuses on the development of the experimental test bed for BPM characterization. Results obtained from the experimental setup are compared with simulation results from the previous chapter.

4.2 Experimental models

Figure 4.1 demonstrates the short section of the beamline, that is the experimental test stand. The short section of the beamline consists of two standard conflat nipples connected to either side of the main BPM flange with bolts. Since the charged particle beam can not be used for the BPM characterization, instead, the beam is represented by a rigid tube of radius $r = 2.35mm$, positioned in the center of the beamline. The radius of the "beam" is chosen to mimic the "pencil beam" in terms of standard, commercially available copper tubing size. Both ends of the beamline are terminated with copper endplates with SMA connectors attached to them. The "beam" is connected to the inner conductor of the SMA connector. Figure 4.1 also points out the presence of copper gaskets inserted in the setup, for better electrical conductivity and Y-X effect reduction as described in Section 3.5.2.

The experimental setup has 3 main ports for measurements: Port 1 (Input Port), Port 2 (Output port) and Port 3 (Pickup port). Although there are four pickup ports, only one of the ports is used due for measurement, because the azimuthal symmetry

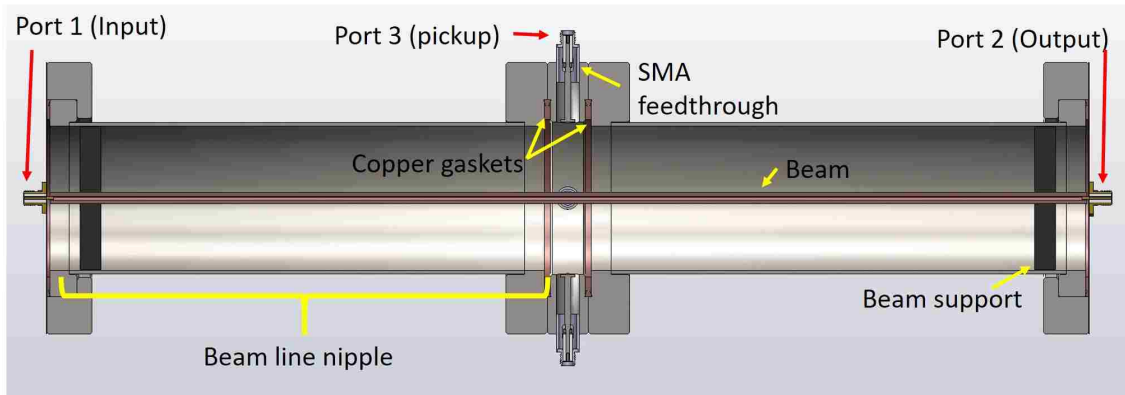


Figure 4.1: The cross section of the experimental setup model.

of pickups in the flange provides identical results.

The operating frequency of the BPM depends on the klystron frequency band [2-4] GHz, but for the purpose of the experimental test bed, the BPM behavior is considered on a wide frequency band [100 MHz - 10 GHz]. The experimental setup is built in two configurations, which are described in the next section.

4.2.1 Experimental Configuration 1

Configuration 1 includes all components described in the previous section. Figure 4.2 shows the parametric representation for Configuration 1.

Figure 4.3 shows a detailed cutout of experimental components, where Figure 4.3 (a) is a zoomed version of Port 1. The beamline is terminated with the copper endplate with the thickness of $t = 0.35mm$. Although not shown the endplate is connected to the conflat nipple with bolts. The SMA connector is soldered to the copper endplate for best electrical conductivity. One side of the "beam" is soldered to the inner conductor of the SMA port. The other side of the "beam" is connected to the inner conductor of the SMA connector via a tight banana plug.

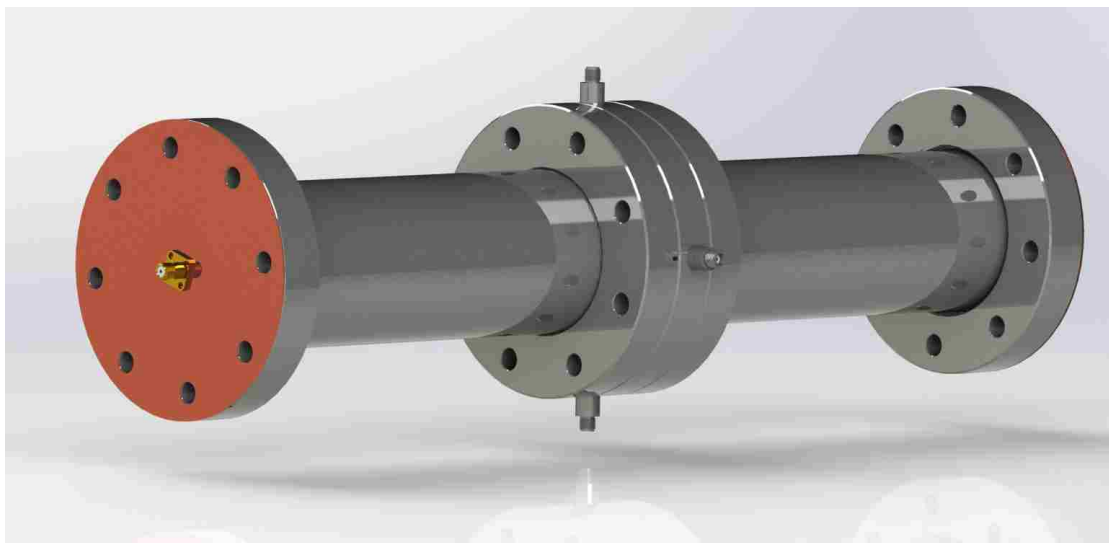
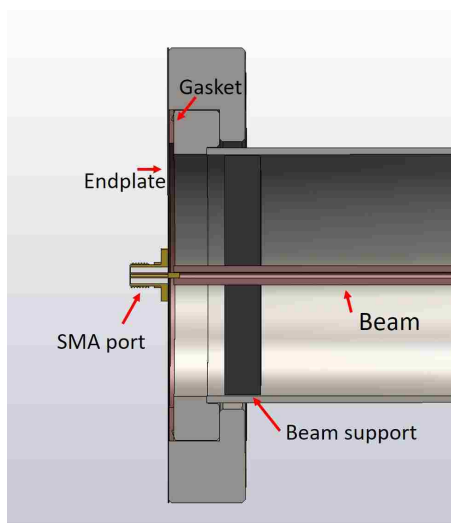
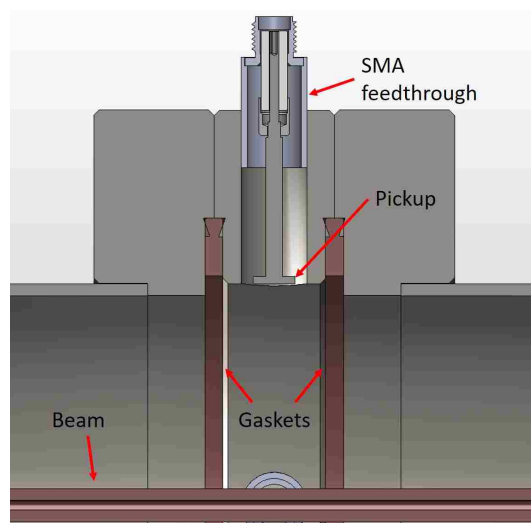


Figure 4.2: The model of the experimental Configuration 1.



(a) Closeup of the end of the experimental Configuration 1.



(b) Closeup of the BPM section in the experimental setup.

Figure 4.3: A detailed cutout of the experimental Configuration 1.

Figure 4.3 (b) shows the model of the BPM flange. The SMA feedthrough is welded to the BPM flange. The inner conductor of the SMA feedthrough is welded to a stem, of the same radius, and also welded to the button pickup.

4.2.2 Experimental Configuration 2

Configuration 2 is constructed in the similar fashion, but with one major difference: conical reducers are attached to each side of the beamline as shown in Figure 4.4. The addition of the conical reducers serves a purpose of minimizing the Y-X effect in the transfer function and pushing the resonance frequency up and out of the experimental frequency range as described in Section 3.5.6

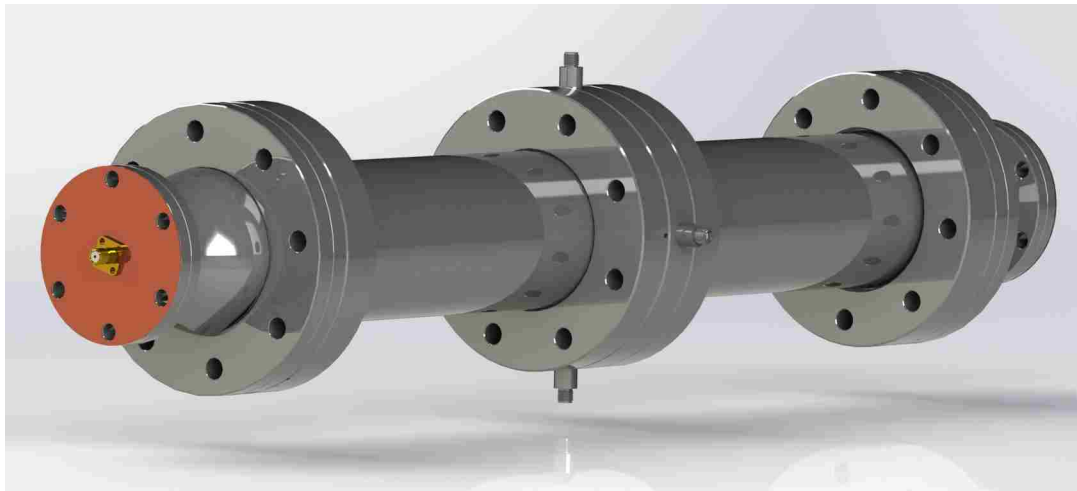


Figure 4.4: The model of the experimental Configuration 2.

Figure 4.5 shows the detailed cross section of the experimental Configuration 2. The conical reducer is attached to the full nipple with copper gasket between them. The smaller side of the cone is terminated with the copper endplate. The SMA connector is soldered to the endplate similarly to the Configuration 1. The behavior of BPM transfer function is expected to be similar for both experimental

configurations, but due to the increased length of the configuration 2, the number of standing waves is expected to increase.

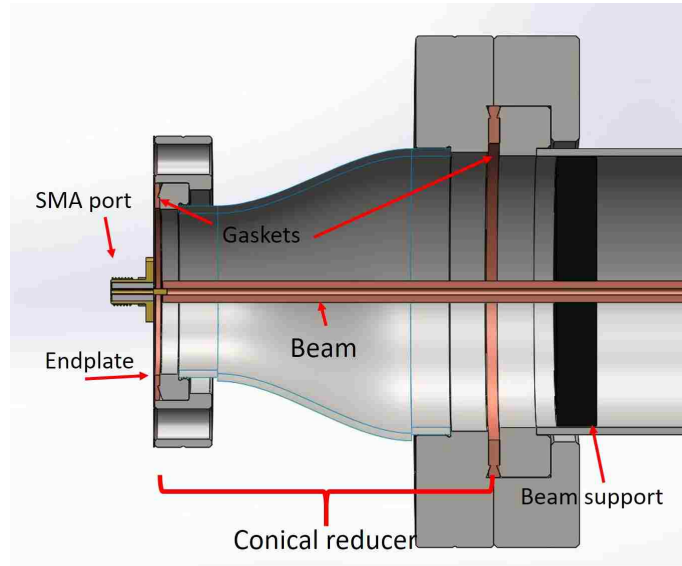


Figure 4.5: The closeup of the experimental Configuration 2.

4.3 Experimental results for Configuration 1

The main goal of the experiment is to measure 3 different S parameters :

1. S_{11} – Measure the reflection at Port 1
2. S_{S21} – Measured transmission from Port 1 to Port 2
3. S_{31} – Measured transmission from Port 1 to Port 3, while Port 2 is properly terminated

The combination of S_{11} and S_{21} parameters shows how well the system is matched. S_{31} parameter is the crucial BPM transfer function measurement. Due to the axial symmetry around the BPM flange in both experimental setups, S_{22} , S_{12} , S_{13} produce

Chapter 4. Experimental analysis

the same results as S_{11} , S_{21} and S_{31} respectively and are not described in this chapter.

For S_{11} and S_{21} measurements the VNA port 1 was connected to Port 1 of the experimental setup and the VNA port 2 was connected to Port 2 of the experimental setup as shown in Figure 4.6. Pickup ports (Port 3) were left untouched.

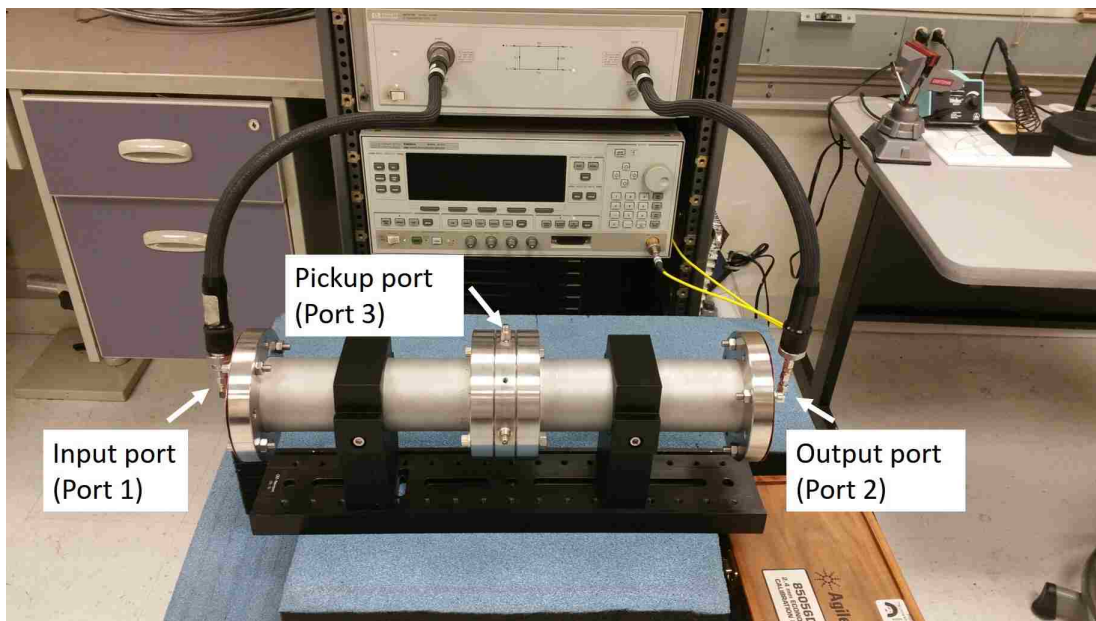


Figure 4.6: The measurement of S_{21} in configuration 1.

Figure 4.7 shows results of S_{11} and S_{21} for the experimental configuration 1. A series of dips/peaks could be observed on the entire frequency range. Such dips/peaks are caused by standing waves in the closed structure as described in Chapter 3. S_{11} and S_{21} look opposite of each other, for every dip in S_{11} , there is a peak at S_{21} and the other way around.

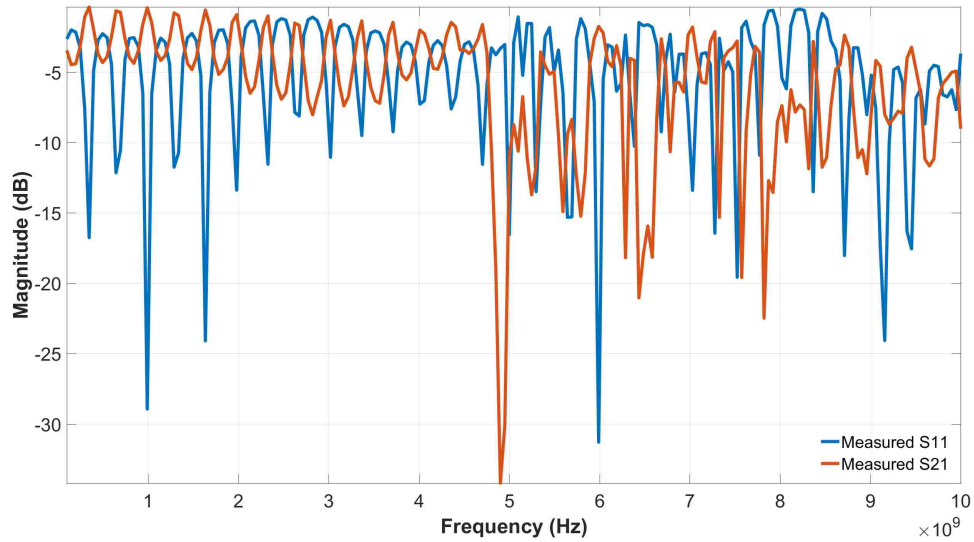


Figure 4.7: Measured S_{11} and S_{21} results in the configuration 1.

The length of the Configuration 1 is 0.435m, which corresponds to the first standing wave to be at 344 MHz. Theoretically, all dips after the first one should correspond to the integer multiples of the first dip frequency. It could also be noticed that there is a large dip in S_{21} is present at around 4.8-4.9 GHz. This major dip is caused by the destructive interference and Y-X effect described in section 3.5.2. Another important observation can be made, that the value of S_{21} is decreasing at high frequencies due to the skin effect in stainless steel.

For S_{31} parameter measurement, the connection of the VNA port 1 was left connected to the Port 1 of the experimental setup. The VNA port 2 was connected to the Port 3 of the experimental setup (pickup port). The Port 2 of the experimental setup was terminated with a 50 Ohm load as shown in Figure 4.8. When S_{11} from Figure 4.6 compared to S_{11} from Figure 4.8, results are completely overlapped, proving the validity of the proper 50Ω termination.

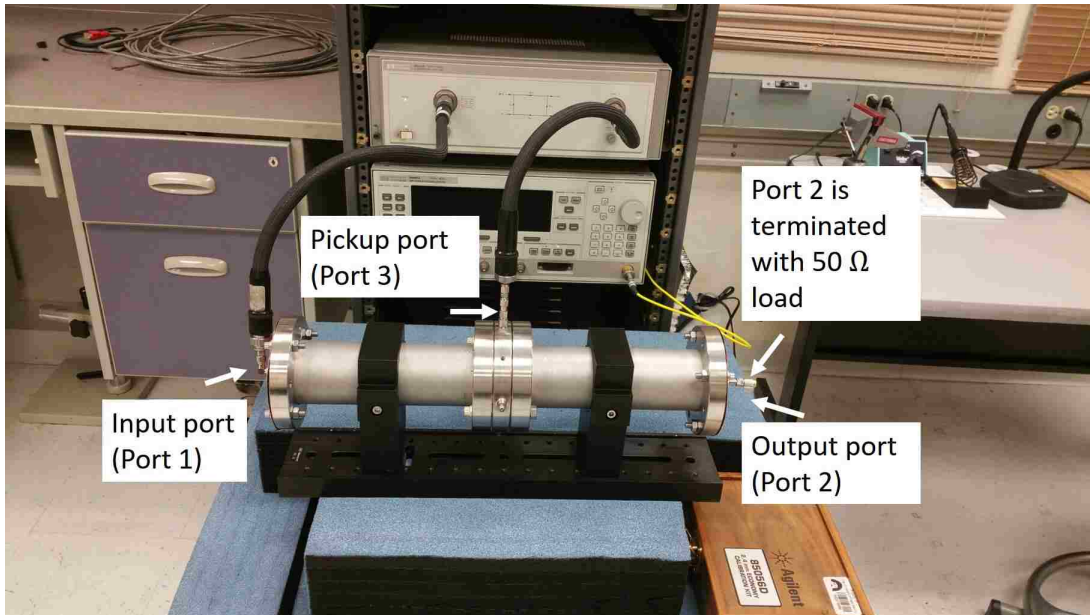


Figure 4.8: The measurement of S_{31} in the experimental Configuration 1.

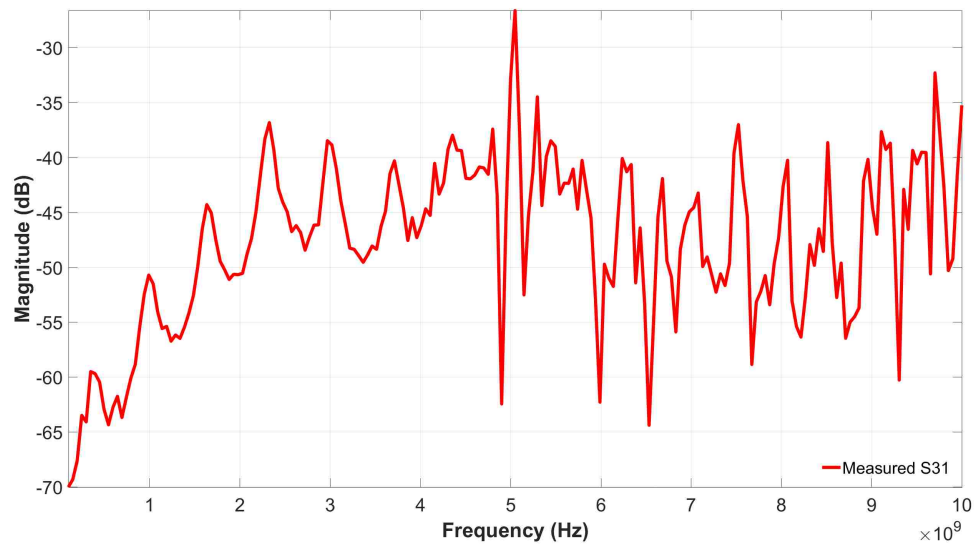


Figure 4.9: Measured S_{31} result in the Configuration 1.

Figure 4.9 shows the experimental result of S_{31} measurement. The measurement shows the transfer function of the BPM pickup. S_{31} result is distorted by the presence

of standing waves in the structure. The transfer function starts at a very large negative value at low frequencies. In the mid frequency range 3-5 GHz the transfer function is oscillating around -40 dB and at frequencies above 6 GHz the value of the transfer function is decreasing, most likely due to the lower S_{21} value.

4.4 Experimental results for Configuration 2

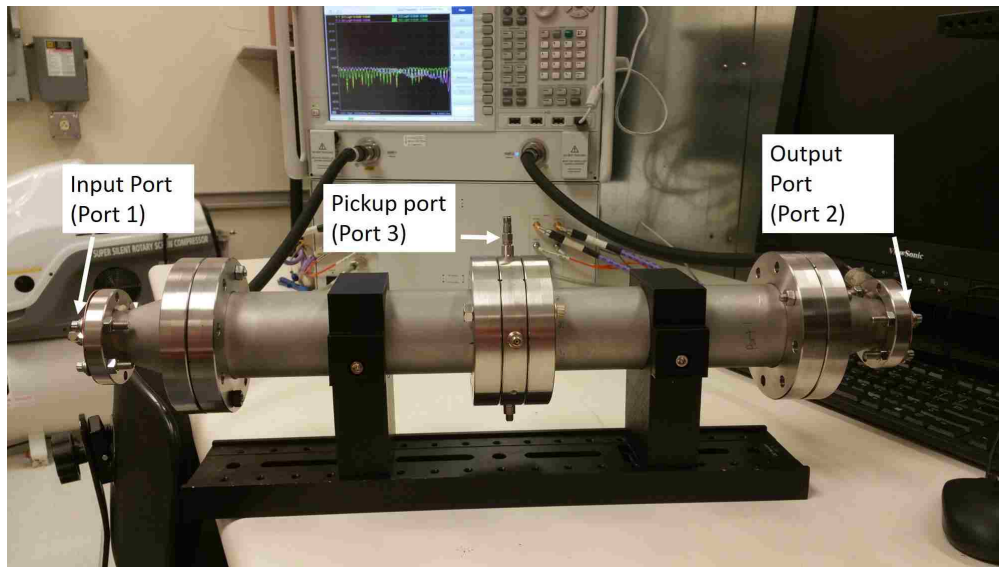


Figure 4.10: The measurement of S_{11} and S_{21} in Configuration 2.

The purpose of the experimental Configuration 2 was mainly to reduce the Y-X effect and push the destructive interference out of the experimental frequency range.

The result of S_{21} in Configuration 1 showed to have the large dip at around 4.9 GHz, indicating the destructive interference at that frequency. The conical reducers were used to gradually decrease the Y-X effect, and push the resonant frequency higher than the operating frequency range.

Chapter 4. Experimental analysis

The experimental configuration 2 used the same nomenclature for identifying ports as shown in Figures 4.10 and 4.12.

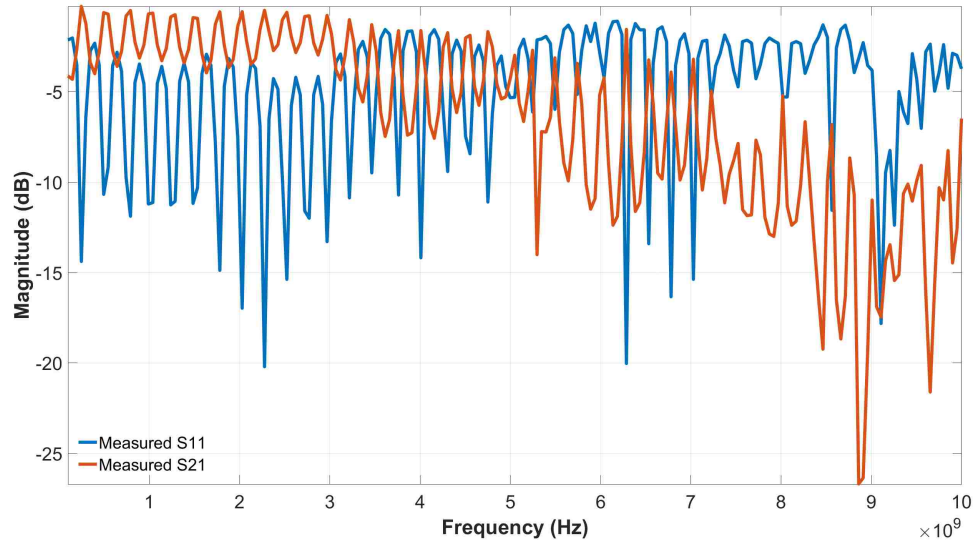


Figure 4.11: Measured S_{31} result in the Configuration 1.

Figure 4.11 shows the experimental result for S_{11} and S_{21} for the experimental configuration 2. It could be observed that the standing waves appear to be present in this configuration as well.

The length of the experimental configuration 2 was increased to 0.58 m due to cones. The first dip of the standing wave was expected to be observed at 258 MHz. Since the standing wave frequency decreased the number of standing waves increased in the long structure. The large dip in S_{21} got shifted from 4.9 GHz to almost 9 GHz due to the Y-X effect reduction.

Lastly the experimental configuration 2 was connected in the same manner as configuration 1 for S_{31} measurement as shown in Figure 4.12. The Port 2 was terminated with 50Ω load.

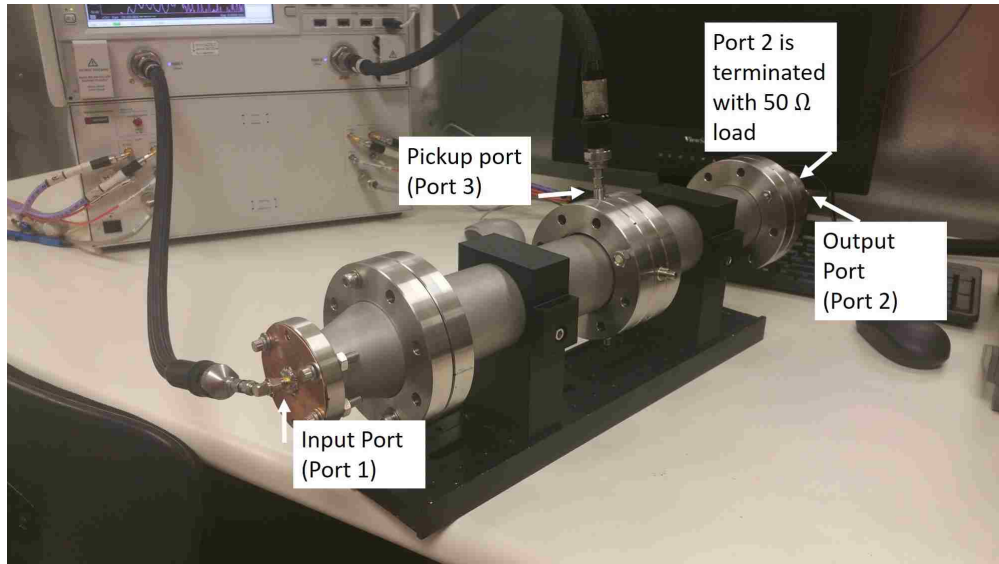


Figure 4.12: The measurement of S_{31} in Configuration 2

Figure 4.24 shows the transfer function of the BPM in the experimental configuration 2. The transfer function has the similar shape as the configuration 1, but with lower amplitude of dips.

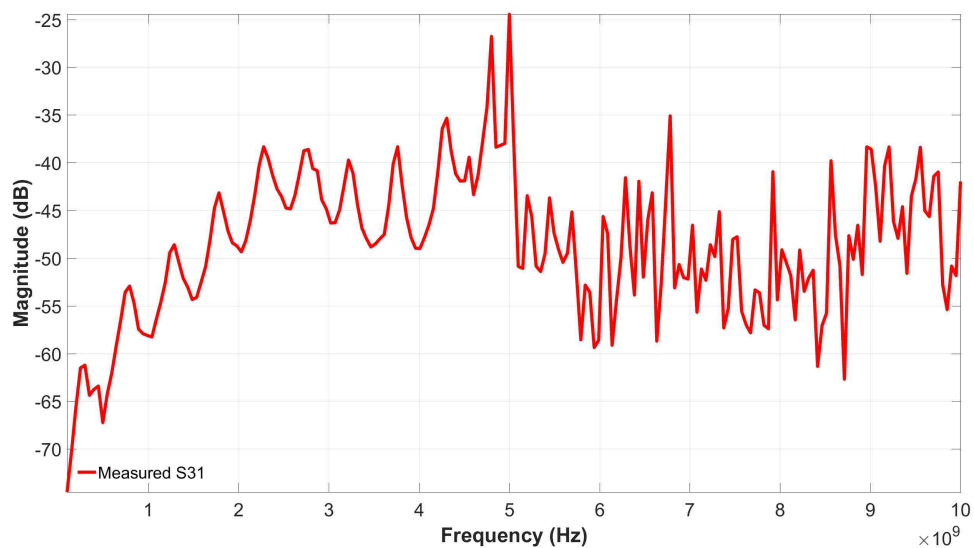


Figure 4.13: Measured S_{31} result in the Configuration 1.

4.5 The experimental result comparison

After collecting experimental results, the comparison needs to be made with transfer functions described in Chapter 3. The comparison is done for S_{11} , S_{21} and S_{31} .

4.5.1 The result comparison for Configuration 1

The result comparison of S_{11} is shown in Figure 4.14. It could be noticed that both measured and simulated S11 results have similar shapes, yet dips do not quite overlap. There is a noticeable shift in frequency. The first dip appears to be at 350 MHz and simulated results overlap with measured results.

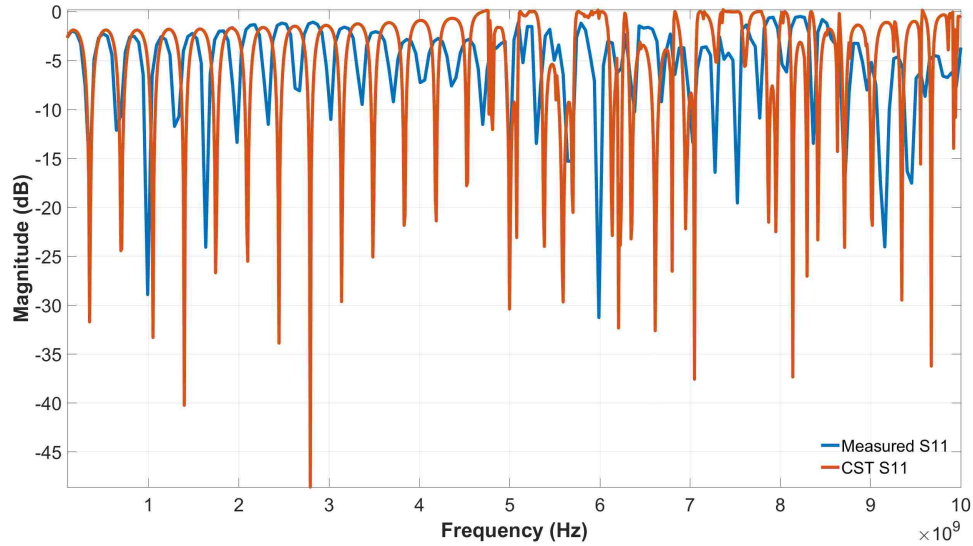


Figure 4.14: Measured vs simulated S_{11} results comparison for the experimental Configuration 1.

The difference in the frequency shift is also not consistent throughout the experimental frequency range. Figure 4.15 shows S_{11} comparison, where simulated result was shifted to the left by 100 MHz. When the simulation result is shifted, dips in the range [2-4] GHz overlap nearly identically, while the first dip does not overlap.

Chapter 4. Experimental analysis

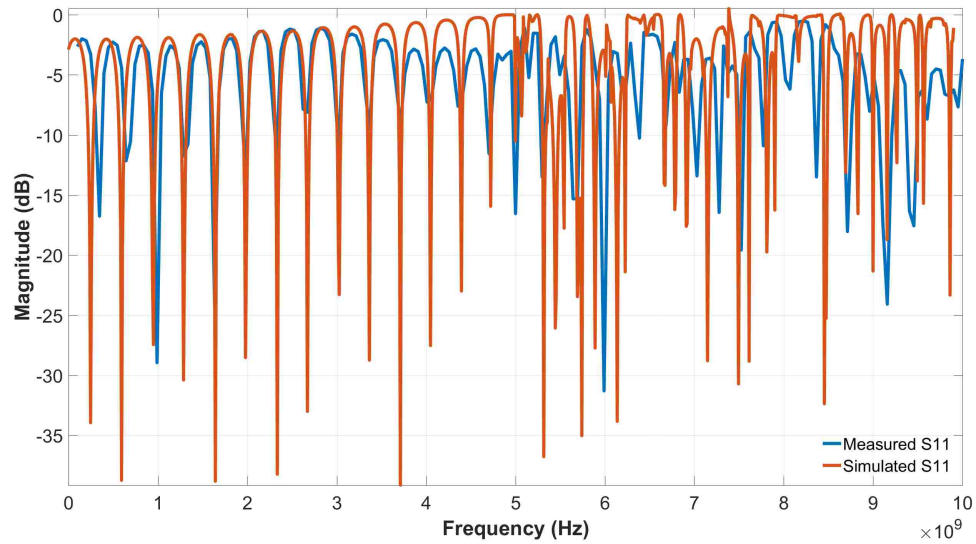


Figure 4.15: Measured vs simulated S_{11} results comparison for the experimental configuration 1. The simulated plot is shifted 100 MHz to the left

The next comparison was done with S_{21} of the configuration 1.

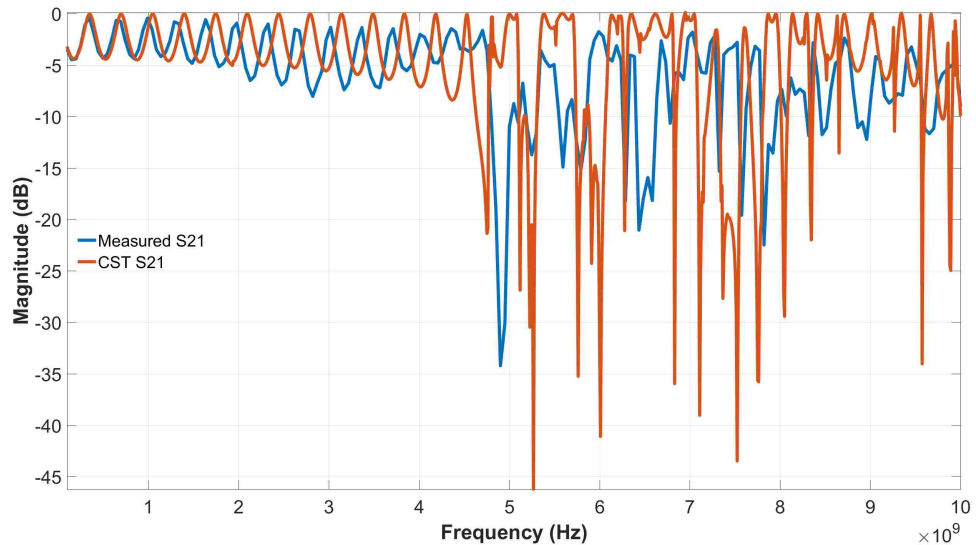


Figure 4.16: Measured vs simulated S_{21} results comparison for the experimental Configuration 2.

Chapter 4. Experimental analysis

Similarly to S_{11} results, simulated S_{21} results could be shifted by 100 MHz to the left as well. The result of the frequency shift is shown on Figure 4.17. S_{21} experimental measurements features the large dip in transmission at about 5 GHz. The simulated result with a 100 MHz shift also overlaps that feature. **Section 3.5.2 analytically predicts the Y-X destructive interference to occur at about 4.6 GHz. The experimental result demonstrates the dip at around 4.8-4.9 GHz, which is very close to the calculated frequency value.**

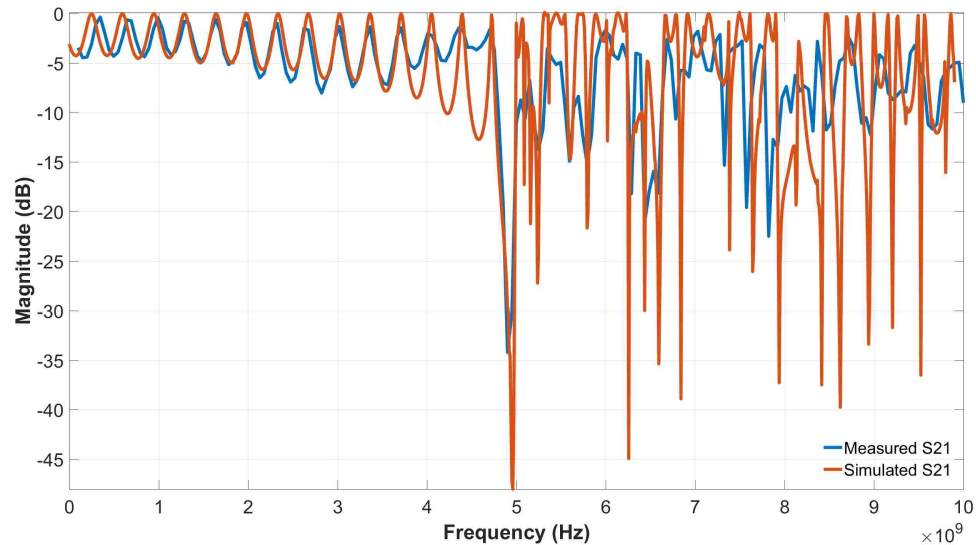


Figure 4.17: Measured vs simulated S_{11} results comparison for the experimental Configuration 1. The simulated plot is shifted 100 MHz to the left.

The result comparison for S_{31} is shown in Figure 4.9. Similarly to previous results the first peak of experimental and simulated results is overlapped in frequency, but the amplitude of transfer functions are not matched.

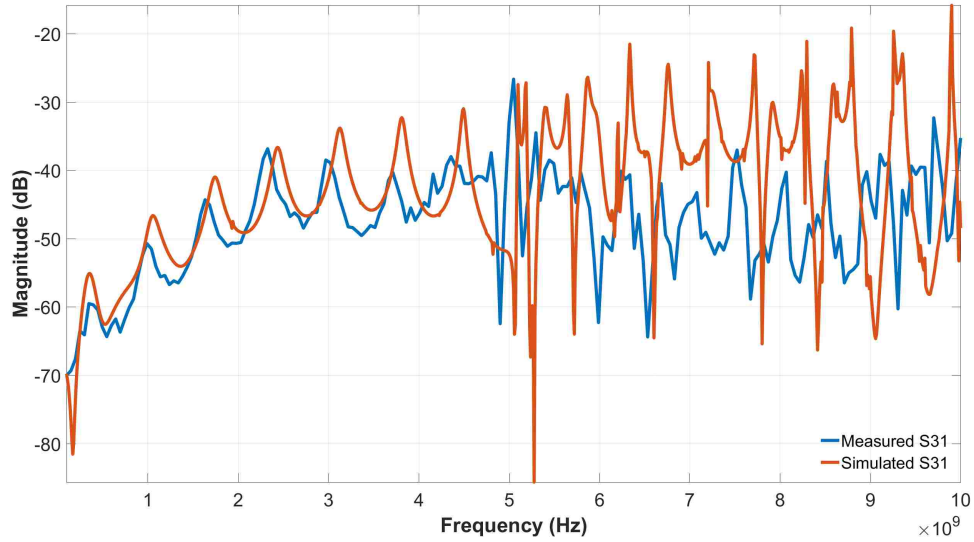


Figure 4.18: Measured vs simulated S_{31} results comparison for the experimental Configuration 1.

The amplitude difference could be caused mainly by the imperfections of the experimental setup. As discussed in Chapter 3, the magnitude shift of transfer function is caused by change in C_{pickup} , which depends on the recessed and protruded deviations of the button in the BPM flange.

The frequency shift of 100 MHz was also performed on S_{31} results as shown in Figure 4.19. There could be noticed the reduction in the amplitude at higher frequencies. As noted before this is caused by the skin effect of the stainless steel. The simulation result shows fairly consistent values at frequencies above 5 GHz.

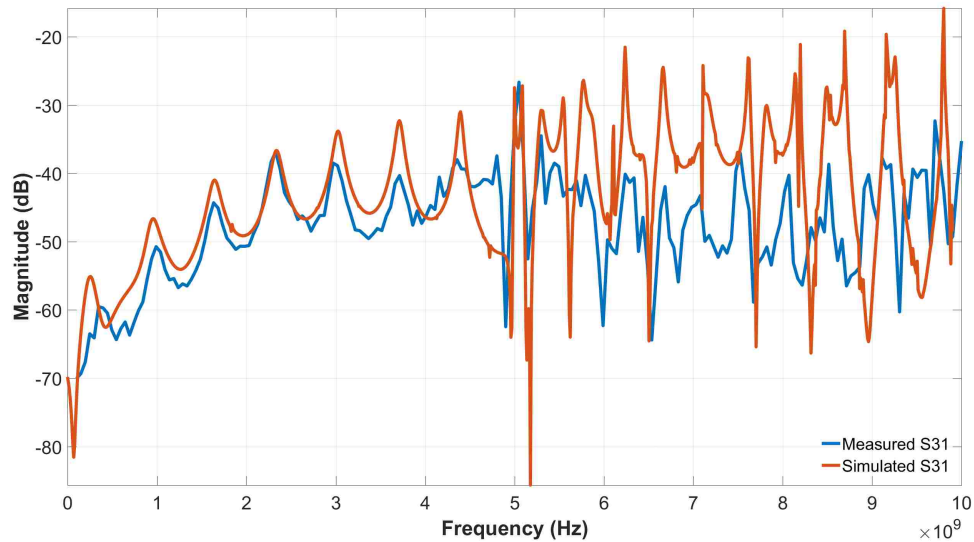


Figure 4.19: Measured vs simulated S_{31} result comparison. The simulated plot is shifted 100 MHz to the left.

4.5.2 The result comparison for Configuration 2

The configuration 2 results were compared to simulation results and had a very similar conclusion to the configuration 1 results comparison. Figure 4.20 shows the comparison between experimental and simulated results of S_{11} in configuration 2. The first dip would overlap perfectly while the following dips would be offset.

While shifting simulation results to the left by 100 MHz, it could be observed that dips in the range 2-6 GHz overlaps, while dips outside of this range do not overlap well. The result for simulation result shift is shown in Figure 4.21

Chapter 4. Experimental analysis

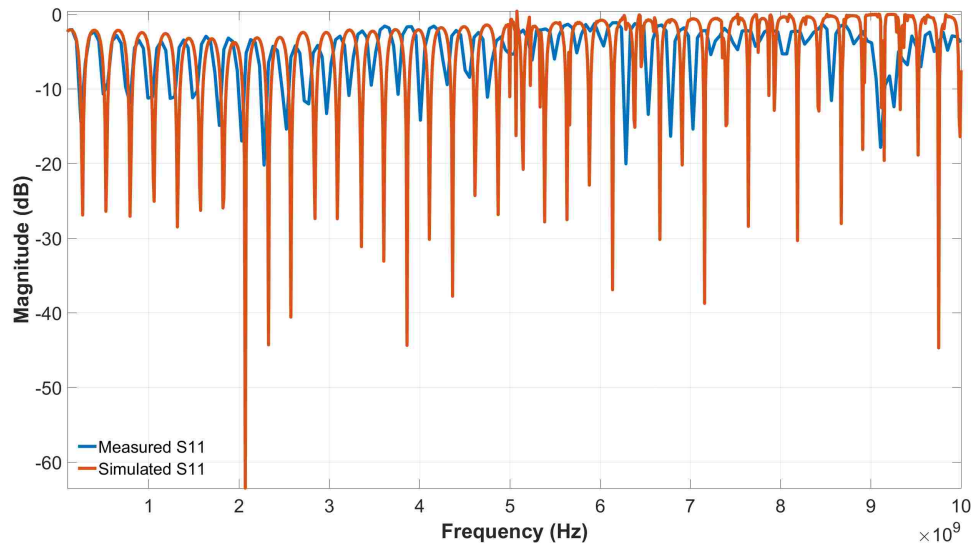


Figure 4.20: Measured vs simulated S_{11} results comparison for the experimental Configuration 2.

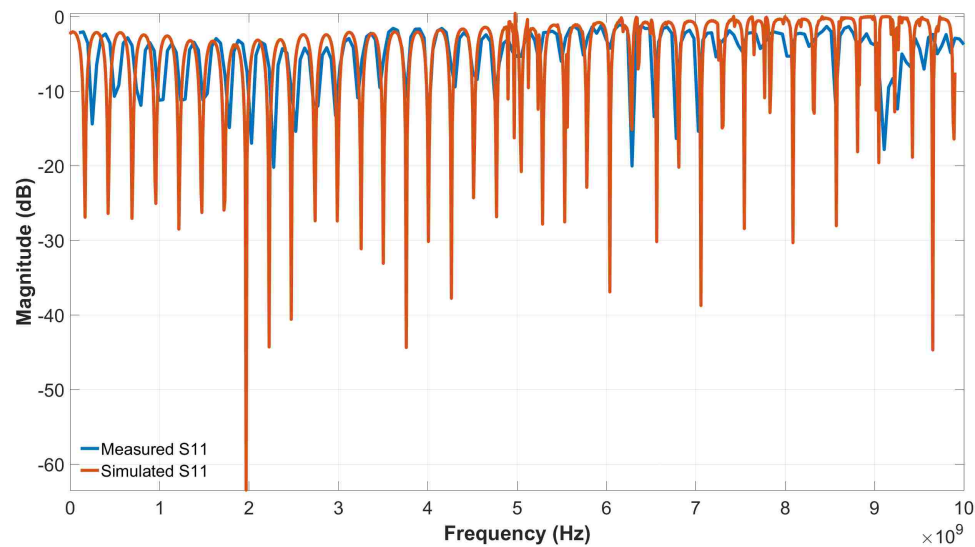


Figure 4.21: Measured vs simulated S_{11} results comparison for the experimental Configuration 2. The simulated result was shifted by 100 MHz to the left

Figures 4.22 and 4.23 show the result comparison between simulated and measured S_{21} parameters. The blue line represents measured S_{21} and the orange line represents

Chapter 4. Experimental analysis

the simulated S_{21} . As discussed before the signal transmission of S_{21} starts to decrease at about 3 GHz. The simulated result, again, shows no overall decrease in the amplitude of S_{21} at high frequencies and it could be concluded that there are losses in the experimental setup due to skin effect.

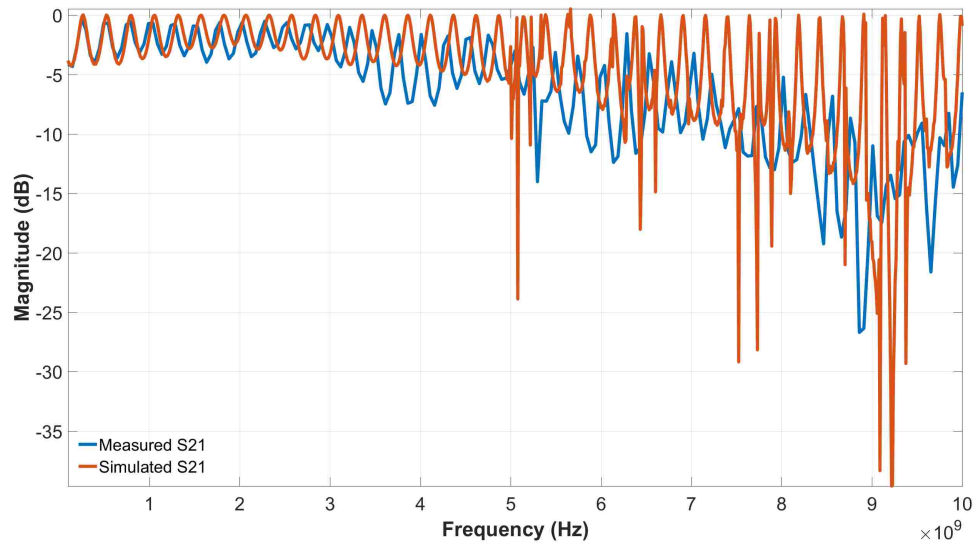


Figure 4.22: S_{21} Measured vs simulated S_{21} results comparison for the experimental Configuration 2.

The major dip that is now present at about 9 GHz is also present in the simulation result of S_{21} , yet even shifted by 100 MHz the major dip of the experimental result did not overlap the simulation result as shown in Figure 4.23.

Chapter 4. Experimental analysis

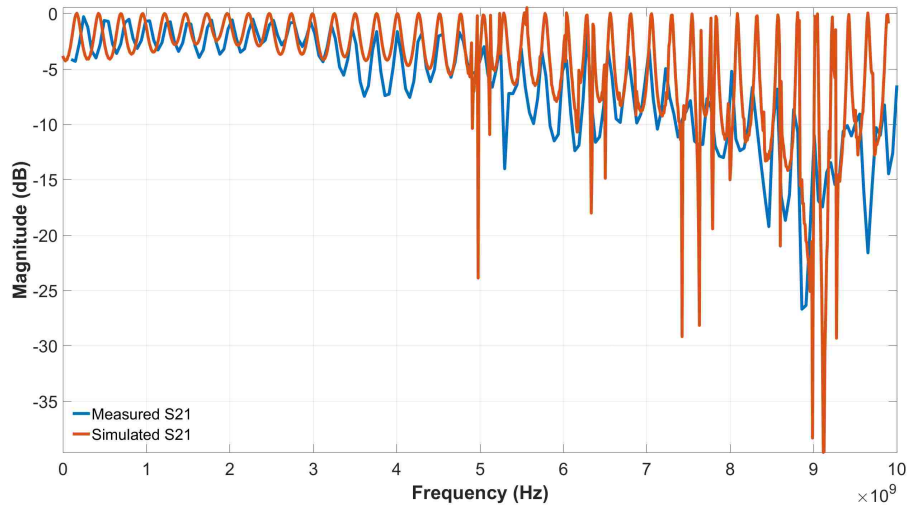


Figure 4.23: Measured vs simulated S_{21} results comparison for the experimental configuration 2. The simulated result was shifted by 100 MHz to the left.

Figure 4.24 shows the comparison between the experimental S_{31} and the simulated S_{31} results. The comparison shows overlapping results at low frequencies up to 3 GHz.

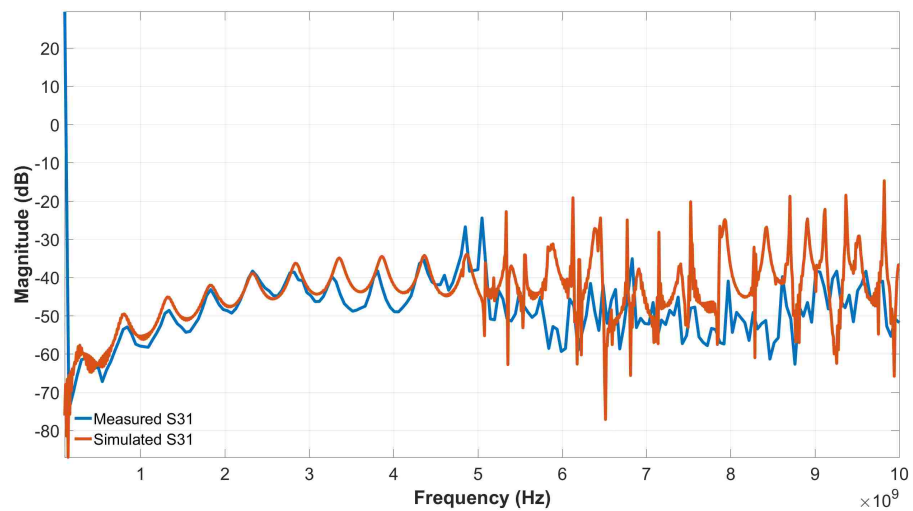


Figure 4.24: Measured vs simulated S_{31} results comparison for the experimental Configuration 2.

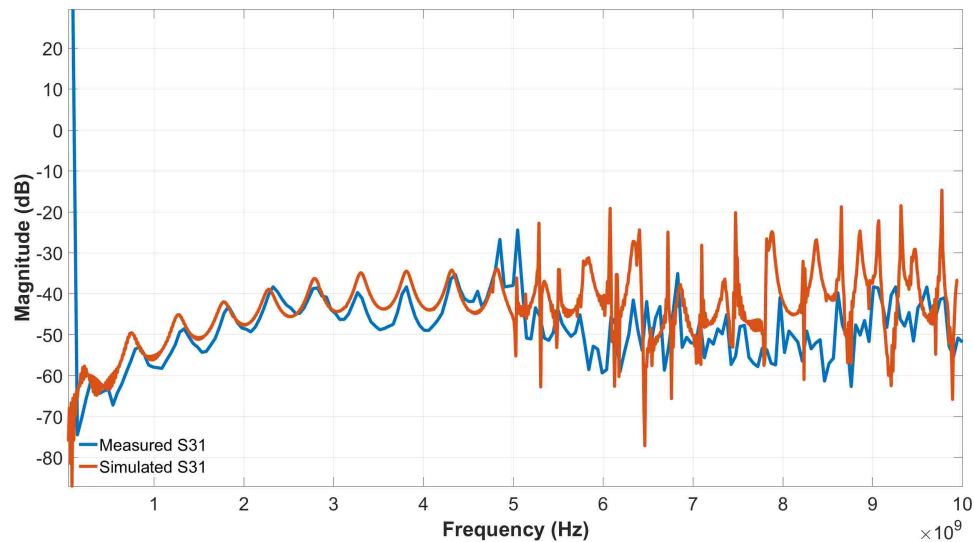


Figure 4.25: Measured vs simulated S_{31} results comparison for the experimental Configuration 2. The simulated result was shifted by 100 MHz to the left.

4.6 Summary and conclusion

The goal of Chapter 4 was to describe the experimental test stand and perform S-parameter measurements in the laboratory. The experimental setup included a short section of a linac beamline with the BPM flange. The rigid rod was used to mimic a particle beam. Both ends of the beamline section had to be terminated to connect the measuring equipment.

The experimental goal was to achieve 3 types of measurements: S_{11} , S_{21} and S_{31} . The combination of S_{11} and S_{21} shows how well the system is match at ports. S_{31} was the crucial measurement of the BPM pickup transfer function. The Vector Network Analyzer (VNA) was used to perform S-parameter measurements on the range 100MHz-10 GHz.

Two models of the experimental test stand were presented and described:

Chapter 4. Experimental analysis

- 1) The configuration model 1 included only the BPM flange, two full nipples and copper endplates
- 2) The configuration model 2 included the BPM flange, two full nipples, two conical reducers and copper endplates.

The configuration 1 and the configuration 2 are both closed systems with the point of the impedance mismatch. In the closed system standing waves are expected to be observed. The configuration 1 has the length of 0.435 m, which corresponds the first standing wave to occur at 344 MHz. The remaining standing waves in the frequency range correspond to the frequency of the integer multiples of the first standing wave frequency.

The configuration 2 has the length of 0.58 m and the first standing wave is expected to happen at 258 MHz. Similarly to the configuration 1, all remaining standing wave frequencies will correspond to the integer multiples of the first standing wave frequency.

The simulation vs experimental measurement result comparison showed a slight deviation of results. The first dip/peaks were overlapped, however the remaining standing waves frequencies were 100-200 MHz ahead. Simulated results were shifted by 100 MHz at each case demonstrating nearly identical results for each comparison. The nature of the frequency shift is yet unexplained and needs to be addressed more.

The configuration 1 demonstrated a very noticeable Y-X effect, described in Section 4.5.2 at 4.9 GHz. The destructive interference reduced the magnitude of S_{21} to nearly -40 dB at 4.9 GHz. In order to push the dip, the Y-X value had to be minimized and the conical reducers were introduced. The reduced value of Y-X increased the frequency of the destructive interference to about 9 GHz, which is away from the S band.

Chapter 4. Experimental analysis

The S_{31} measurements closely correlate to simulated transfer functions. The transfer function for the experimental configuration 2 has less oscillations due to the lower frequency of standing waves (longer construction). Also due to the lower Y-X value the destructive interference frequency has less effect on S_{31} measurement.

Chapter 5

Conclusion and future work

5.1 Introduction

Los Alamos National Laboratories has designed and constructed a Beam Position Monitor (BPM) for linear accelerator in the Mo-99 production facility. The purpose of this thesis was to fully characterize this BPM, analytically, experimentally and via numerical simulations .

Chapter 2 focused on the derivation of the analytical transfer curve of the Beam position monitor system from first mathematical and physical principles.

Chapter 3 focused on the development of finite element time and frequency domain numerical simulation models of the BPM system

Chapter 4 focused on the design and build of an experimental test bed for laboratory characterization of the BPM diagnostic.

A summary of the key finding is presented below along with future work that could be done to improve the BPM characterization test stand.

5.2 An analytical description of the BPM system

Chapter 2 focuses on the mathematical derivation of the BPM transfer function and resultant voltage induced on the pickups. A BPM system is a collection of capacitive sensors (pickups), positioned flush with the inner surface of the beamline. While the particle beam drifts past these sensors, the time dependent electric field of the beam couples to the BPM pickups on the surface of the beam line inducing a voltage signal

Chapter 5. Conclusion and future work

on each pickup. The combined differential signals from opposing pickup determine the spatial position of the beam.

Based on the detailed BPM schematic, defined in Section 2.4, the pickup voltage V_{pickup} was mathematically derived in terms of the pickup current I_{pickup} and the transient impedance of a single pickup Z_t . The derivation showed that the pickup worked in two regimes for $\omega \ll \omega_c$ and $\omega \gg \omega_c$, where ω is the operating frequency and ω_c is the cutoff frequency. The mathematical derivation of V_{pickup} holds for the beam being in the center; however, if the center condition is not met a new derivation is required for each new displacement of the beam from center, which is not ideal for a BPM characterization. In order to simplify the characterization process, an additional characterization model was proposed: an equivalent circuit model. The circuit model depended on 3 variables: C_{pickup} - the capacitance between the pickup and the beam, C_{stray} - the parasitic capacitance between the pickup and the BPM flange and R_c the characteristic impedance of the SMA feedthrough. The transfer function of the equivalent circuit, shown below, provided the required characterization information for a wide frequency range.

$$H(s) = \frac{sR_c C_{pickup}}{sR_c(C_{stray} + C_{pickup}) + 1} \quad (5.1)$$

The transfer function derivation completed the analytical part of the characterization process. The next step in the characterization was to verify the transfer function using a finite element and SPICE models as well as compare with experimental measurements.

5.3 Numerical simulation models

Chapter 3 focuses on the development of several numerical simulation models of the Beam Position Monitor system: 1) an electrostatic model, 2) a SPICE model and 3) time domain and frequency domain models.

The first goal was to develop an electrostatic model to accurately simulate values for C_{pickup} and C_{stray} . The model captured a geometry of the BPM and iteratively solved for field values as well as energy values from, which the capacitance values were calculated. The capacitance value of C_{pickup} was very close to analytically approximated number in Chapter 2. The simulated capacitance value for C_{stray} was nearly 4 times larger than the analytically derived capacitance due to an abundance of fringing fields.

The capacitance results were used in SPICE model to produce a transfer curve of a BPM equivalent circuit. Additionally a time domain finite element model of the BPM in a beamline with a centered current density was implemented, utilizing high conformal cell density near the pickups and perfect boundary layers at the entrance and outlet of the beam line to simulate an infinitely long coaxial cylinder. The results of the time domain model were compared to the transfer function of the BPM equivalent circuit from the SPICE simulation. The result comparison showed a slight result disagreement in the magnitude, by about 5 dB. Both, time domain and SPICE simulations, were repeated multiple times with various parameter changes. The difference in magnitude by 5 dB remained present. Despite a minor magnitude disagreement shapes and cutoff frequencies were the same. The transfer function proved to be a reliable way for a BPM characterization.

Along with the frequency domain model of the infinite beamline with BPM a frequency domain model of the experimental test bed was developed. The experimental test stand is comprised of multiple components with specific dimensions and multiple details, which could reflect on the transfer function results. In order to account

for all details a step-by-step procedure was described. The description started with a perfectly matched canonical transmission line. The geometrical complexity was increased with every step, however the effects from each step were explained in detail. Finally a full experimental setup was described and results of the transfer function were discussed. The last step of the characterization was to perform experimental measurements and compare them to the numerical model.

5.4 The experimental setup

Chapter 4 describes the experimental test stand and experimentally obtained S-parameters measured in the laboratory. The experimental setup includes a short section of a linac beamline with the BPM flange. A rigid rod was used to mimic a particle beam. Both ends of the beamline section had to be terminated to connect the measuring equipment. Obviously in the following configuration, the position of the beam is invariant, always centered. The position and curvature of the rod was minimally offset from center. This allows for complete characterization of the diagnostic and comparison with the analytical and numerical simulation models.

The experimental goal was to conduct 3 types of S parameter measurements: S_{11} , S_{21} and S_{31} . The combination of S_{11} and S_{21} shows how well the system is matched at the ports. S_{31} was the crucial measurement of the BPM pickup transfer function. A Vector Network Analyzer (VNA) was used to perform these measurements, which were carried from 100 MHz to 10 GHz.

Two different configurations were setup in the test bed :

- 1) Configuration 1 consisted of the BPM flange, beamline section and copper endplates
- 2) The configuration model 2 consists of the BPM flange, beamline section, two

Chapter 5. Conclusion and future work

conical reducers and copper endplates.

Configuration 1 and configuration 2 are both terminated with copper endplates with 50 Ohm SMA ports soldered to them. Based on the analysis done in Section 3.5.6 standing waves were expected in both configurations. Based on the length of the configuration 1 the first resonant frequency was calculated to be 344 MHz and the experimental result supported the calculation. Similarly to the configuration 1, the configuration 2 calculations were also supported by experimental results.

The simulation vs experimental measurement result comparison showed a slight deviation of results. The first dip/peaks overlapped, however the remaining standing waves frequencies were 100-200 MHz ahead. In order to overlap results, simulated results were shifted by 100 MHz and dips/peaks from were nearly identical. The shift persisted through all measured results; however the nature of the frequency shift is yet unexplained could be a part of an experimental or a simulation artifact.

Configuration 1 demonstrated a very noticeable Y-X effect, described in Section 4.5.2 at 4.9 GHz. The destructive interference reduced the magnitude of S_{21} to nearly -40 dB at 4.9 GHz. In order to push the dip, the Y-X value had to be minimized and the conical reducers were introduced. The reduced value of Y-X increased the frequency of the destructive interference to about 9 GHz, which is away from the S band.

The S_{31} measurements closely correlate to the simulated transfer function. The transfer function for the experimental configuration 2 has less oscillations due to longer electrical length and due to the lower $Y - X$ length, which makes the configuration 2 a better experimental test stand for the BPM characterization.

5.5 Future work

While the goal of the project was achieved there are some improvements that could be made in future work. The main enhancement could be done to the experimental setup by accomplishing these steps:

1. **Add the beam position variability in the experimental setup** The principal challenge of the experimental setup was matching of the beam-beamline combination to the 50Ω connector in order to mitigate signal reflections. In order to have a complete experimental characterization of the diagnostic it is important to have spatial variability of the beam from the center but this is nearly impossible to create in the existing experimental setup. Perhaps a different design that incorporates specially designed endplates to hold the beam might work
2. **Create a map of BPM readings in various beam positions.** Based on the beam spatial variability the map of the signal values could be created and recorded. These values could be later used for a quick comparison and beam position identification.

References

- [1] G.-A. Voss, “Obituaries: Rolf Wideröe”, *Physics Today*, vol. 50, pp. 78-79, 1997.
- [2] V. J. Molinski, “A review of ^{99m}Tc generator technology”, *The International Journal of Applied Radiation and Isotopes*, vol. 33, no. 10, pp. 811-819, 1982.
- [3] R. P. Spencer, “Radioactive isotopes in clinical medicine and research”, *Clinical Nuclear Medicine*, vol. 23, p. 725, 1998.
- [4] A. J. Mundt and J. C. Roeske, “Principles of radiation oncology”, in *Oncologic Therapies*, pp. 9-17, Springer, 2003.
- [5] S. A. Leibel, Z. Fuks, M. J. Zelefsky, S. L. Wolden, and Rosenzweig, *Intensity-Modulated Radiotherapy*, vol. 8. LWW, 2002.
- [6] M. Ahmad, G. Vandegrift, and P. Cristini, “Molybdenum-99 (^{99}Mo): Past, present, and future”, *Science and Technology of Nuclear Installations*, vol. 2013, pp. 1-3, 2013.
- [7] A. Schaper, *Highly enriched uranium, a dangerous substance that should be eliminated*, vol. 124. DEU, 2013.
- [8] B. Edward, “Non-HEU production technologies for Molybdenum-99 and Technetium-99m”, *International Atomic Energy Agency*, 2013.
- [9] G. E. Dale, S. A. Baily, K. A. Bishofberger, and D. A. Dalmas, “Current activities at los alamos national laboratory supporting electron accelerator production of Mo-^{99} ”, Tech. Rep. LA-UR-16-28338, Los Alamos National Laboratory (LANL), 2017.
- [10] H. V. Ruiz, “Production technologies for Molybdenum-99 and Technetium-99m”, *IAEA Rept., TECDOC-1065, Austria*, 1999.

REFERENCES

- [11] K. A. Bishofberger, “Moly99 production facility: Report on beamline components, requirements, costs”, Tech. Rep. LA-UR-15-29675, Los Alamos National Laboratory (LANL), 2015.
- [12] S. R. Smith, A. Lumpkin, and C. E. Eyeberger, “Beam position monitor engineering”, in *AIP Conference Proceedings*, vol. 390, pp. 50-65, AIP, 1997.
- [13] P. Forck, P. Kowina, and D. Liakin, “Beam Position Monitors”, *CERN accelerator school on beam diagnostics*, pp. 187-228, 2008.
- [14] R. E. Shafer, “Beam Position Monitoring”, in *AIP conference proceedings*, vol. 249, pp. 601-636, AIP, 1992.
- [15] M. Cohen-Solal, “Design, test, and calibration of an electrostatic beam position monitor”, in *Physical Review Special Topics-Accelerators and Beams*, vol. 13, pp. 1-13, 2010.
- [16] F. Marcellini, M. Serio, A. Stella, and M. Zobov, “Daφne broad-band button electrodes”, *Nuclear Instruments and Methods in Physics Research Section A: Accelerators, Spectrometers, Detectors and Associated Equipment*, vol. 402, pp. 27-35, 1998.
- [17] Y. Y. Iossel, É. Kochanov, and M. G. Strunskii, “Calculation of electrical capacitance [in Russian]”, Tech. Rep. FTD-MT-24-269-70, Foreign Technology Division, 1969.
- [18] S. Hiramatsu, “Beam position monitors for circular accelerators”, in *Proceedings of IBIC2012*, vol. 1, pp. 590-601, KEK, 2012.
- [19] CST Microwave Studio, “Workflow & solver overview”, *A discretization method for the solution of Maxwells equations for six-component Fields*, pp. 29-45, 2008.

REFERENCES

- [20] G. Sloggett, N. Barton, and S. Spencer, “Fringing fields in disc capacitors”, *Journal of Physics A: Mathematical and General*, vol. 19, no. 14, p. 2725, 1986.
- [21] J. H. Ryu, “Eletromagnetic simulation of initially charged structures with a discharge source”, *Progress in Electromagnetics Research M*, vol. 16, pp. 95-104, 2011.
- [22] D. Pozar, *Microwave Engineering*. Wiley, 4 ed., 2004.
- [23] H. Flugel and E. Kuhn, “Computer-aided analysis and design of circular waveguide tapers”, *IEEE Transactions on Microwave theory and Techniques*, vol. 36, pp. 332-336, 1988.